Exploring the Possibility of Identifying Hydride and Hydroxyl Cations of Noble Gas Species in the Crab Nebula Filament

The Astrophysical Journal, 902:131 (30pp), 2020 October 20 https://doi.org/10.3847/1538-4357/abb5fe

Exploring the Possibility of Identifying Hydride and Hydroxyl Cations of Noble Gas Species in the Crab Nebula Filament

Ankan Das[1], Milan Sil[1], Bratati Bhat[1], Prasanta Gorai[2,1], Sandip K. Chakrabarti[1], and Paola Caselli[3]
[1] Indian Centre for Space Physics, 43 Chalantika, Garia Station Road, Kolkata 700084, India; ankan.das@gmail.com
[2] Department of Space, Earth & Environment, Chalmers University of Technology, SE-412 96 Gothenburg, Sweden
[3] Max-Planck-Institute for extraterrestrial Physics, P.O. Box 1312, D-85741 Garching, Germany; caselli@mpe.mpg.de
Received 2020 February 10; revised 2020 August 19; accepted 2020 August 21; published 2020 October 21

Abstract

The first identification of the argonium ion (ArH^+) toward the Crab Nebula supernova remnant was proclaimed by Herschel in the submillimeter and far-infrared domains. Very recently, the discovery of the hydro-helium cation (HeH^+) in the planetary nebula (NGC 7027) by SOFIA has been reported. The elemental abundance of neon is much higher than that of argon. However, the presence of neonium ions (NeH^+) is yet to be confirmed in space. Though the hydroxyl radicals (−OH) are very abundant in both neutral and cationic forms, hydroxyl cations of such noble gases (i.e., $ArOH^+$, $NeOH^+$, and $HeOH^+$) are yet to be identified in space. Here, we employ a spectral synthesis code to examine the chemical evolution of the hydride and hydroxyl cations of the various isotopes of Ar, Ne, and He in the Crab Nebula filament and calculate their line emissivity and intrinsic line surface brightness. We successfully explain the observed surface brightness of two transitions of ArH^+ (617 and 1234 GHz), one transition of OH^+ (971 GHz), and one transition of H_2 (2.12 μm). We also explain the observed surface brightness ratios between various molecular and atomic transitions. We find that our model reproduces the overall observed features when a hydrogen number density of $\sim(10^4$–$10^6)$ cm^{-3} and a cosmic-ray ionization rate per H_2 of $\sim(10^{-11}$–$10^{-10})$ s^{-1} are chosen. We discuss the possibility of detecting some hydride and hydroxyl cations in the Crab and diffuse cloud environment. Some transitions of these molecules are highlighted for future astronomical detection.

Unified Astronomy Thesaurus concepts: Chemical abundances (224); Radiative transfer simulations (1967); Supernova remnants (1667); Interstellar medium (847); Diffuse interstellar clouds (380)

1. Introduction

The Crab Nebula, henceforth the Crab (M1 = NGC 1952) is the freely expanding remnant of the historical core-collapse supernova of AD 1054 (SN 1054), which contains both atomic and molecular hydrogen, electrons, and a region of enhanced ionized argon emission. The updated distance to the Crab pulsar from the Sun is 3.37 kpc (Fraser & Boubert 2019), compared with that previously obtained of 2 kpc (Trimble 1968), with R.A. and decl. $05^h34^m31\overset{s}{.}935$ and $+22°0'52\overset{''}{.}19$ respectively (Kaplan et al. 2008). The Crab lies about 200 pc away from the Galactic plane in a region of low density, and it is too young to be contaminated by interstellar or circumstellar material.

Hydrogen atoms are widespread in the universe. It is thus no surprise that hydrogenated species are ubiquitous. The huge abundances of molecular hydrogen could be explained by considering the physisorption process of interstellar grains (Biham et al. 2001; Chakrabarti et al. 2006a, 2006b). Numerous strong H_2-emitting (2.12 μm) knots have been identified in the Crab (Loh et al. 2010, 2011). Though the kinetic gas temperature around the knots of the Crab is around ∼2000–3000 K, Gomez et al. (2012) found that the cold and hot components of the dust temperature can be ∼28 and 63 K, respectively. Richardson et al. (2013) modeled emission features of H_2 in this environment. Due to the presence of strong radiation in the Crab, electrons are highly abundant and can readily convert H atoms into H^-, which eventually react with H atoms again to form H_2 molecules. Though there can be some physisorption as well as chemisorption (Cazaux & Tielens 2004) pathways which may lead to H_2 formation, the majority of the H_2 molecules were formed on the cleanest knot (knot 51) of the Crab by $H + H^-$ reaction (Richardson et al. 2013).

Argon is the third most abundant species in Earth's atmosphere. However, instead of the most common isotope of argon (^{36}Ar, mainly produced by stellar nucleosynthesis in supernovae), in Earth's atmosphere, the ^{40}Ar isotope is more common (mainly produced from the decay of potassium-40 in Earth's crust). In Earth's atmosphere, the isotopic ratio of $^{40}Ar/^{38}Ar/^{36}Ar$ is 1584/1.00/5.30 (Lee et al. 2006). Interestingly, the ratio obtained in the Jupiter family comet, 67P/C-G by the ROSETTA mission using the ROSINA mass spectrometer instrument was similar (they obtained an isotopic ratio of about $^{36}Ar/^{38}Ar \sim 5.4 \pm 1.4$). In the solar wind, the isotopic ratio of $^{40}Ar/^{38}Ar/^{36}Ar$ has been measured to be 0.00/1.00/5.50 (Meshik et al. 2007), whereas in the interstellar medium (ISM), the ^{36}Ar isotope is found to be the most abundant (∼84.6%), followed by ^{38}Ar (∼15.4%) and traces of ^{40}Ar (∼0.025%; Wieler 2002). In line with this fact, Barlow et al. (2013) predicted $^{36}ArH^+$ to have a comparatively higher abundance than $^{40}ArH^+$ or $^{38}ArH^+$. Using the data from the Spectral and Photometric Image REceiver (SPIRE) on the Herschel satellite, they reported $J = 1 \rightarrow 0$ (617.5 GHz) and $J = 2 \rightarrow 1$ (1234.6 GHz) emission of $^{36}ArH^+$ along with the strongest fine-structure component of the OH^+ ion (971.8 GHz) toward the Crab. They predicted the limits of the abundance ratios to be $^{36}ArH^+/^{38}ArH^+ > 2$ and $^{36}ArH^+/^{40}ArH^+ > 4$–5. They also derived the abundance of the argonium ion.

Hydrogen-related ions of noble gas species are very useful tracers of physical conditions (Hamilton et al. 2016). The argonium ion can be used as a unique tracer of H_2 (by anticorrelation) as well as atomic gas (correlation) in specific environments (Barlow et al. 2013; Schilke et al. 2014). Moreover, it would also be a good tracer of the almost purely atomic diffuse ISM in the Milky Way (Neufeld & Wolfire 2016). ^{36}Ar is mainly produced during the core collapse of supernovae by the explosive

nucleosynthesis reactions in massive stars. Excitations of molecules in the Crab mainly occur due to the collision with electrons in the region with density of about $\sim 10^2\,\mathrm{cm}^{-3}$. Schilke et al. (2014) assigned the $J = 1 \leftarrow 0$ transition of both isotopologs of ArH^+ ($^{36}ArH^+$ and $^{38}ArH^+$) in absorption with HIFI on board the Herschel satellite toward numerous prominent continuum sources. For example, they identified both isotopologs ($^{36}ArH^+$ and $^{38}ArH^+$) in Sagittarius B2(M) and only the primary isotopolog ($^{36}ArH^+$) toward Sgr B2(N), W51e, W49N, W31C, and G34.26+0.15. Müller et al. (2015) also detected $^{36}ArH^+$ and $^{38}ArH^+$ in absorption of a foreground galaxy at $z = 0.89$ along two different lines of sight toward PKS 1830–211 with band 7 of the Atacama Large Millimeter/submillimeter Array (ALMA) interferometer. Hamilton et al. (2016) described the excitation of ArH^+ in the Crab by collisions with electrons through radiative transfer calculations and found that the ratio of the $2 \rightarrow 1$ and $1 \rightarrow 0$ emission is consistent with an ArH^+ column density of $1.7 \times 10^{12}\,\mathrm{cm}^{-2}$. Priestley et al. (2017) performed combined photoionization and photodissociation modeling of the ArH^+ and OH^+ emission of the Crab filament subjected to synchrotron radiation and a high flux of charged particles. Their model was able to successfully reproduce the observation of Barlow et al. (2013) when they considered total hydrogen densities between 1900 and $2 \times 10^4\,\mathrm{cm}^{-3}$.

Neon is much more abundant than argon. Though the Herschel survey covers the transition $J = 1 \rightarrow 0$ of NeH^+ at 1039.3 GHz, no NeH^+ transition has yet been reported. Helium is the second most abundant species (after hydrogen) in the universe, having an abundance 1/10 relative to hydrogen nuclei. Because argon, neon, and helium are noble gases, they do not normally form stable molecules, but they can form stable ions. A few hundred thousand years after the Big Bang, when the universe cools sufficiently below 4000 K, helium was the first neutral atom produced in the universe, due to it having the highest ionization potential, and so it can be neutral at higher temperatures than hydrogen. Shortly after the first helium atom formed, the first chemical bond in the universe formed through the radiative association reaction between the neutral He atom and a proton. They formed HeH^+ with the emission of a photon. Due to this fact, HeH^+ is considered to be the first molecular ion formed in the universe, and its bond is considered to be the first chemical bond of the universe (Lepp et al. 2002; Galli & Palla 2013).

The helium hydride ion, HeH^+ was first identified in the laboratory nearly 100 yr ago (Hogness & Lunn 1925), and its existence in the ISM was first speculated in the 1970s (Black 1978). Despite these early measurements and predictions, HeH^+ has only recently been detected in space for the first time. Güsten et al. (2019) reported the first astrophysical identification of HeH^+ based on advances in terahertz spectroscopy and high-altitude observation using the German REceiver for Astronomy at Terahertz frequencies (GREAT) facility on the Stratospheric Observatory for Infrared Astronomy (SOFIA). They identified HeH^+ by its rotational ground-state transition at a wavelength of 149.137 μm (2010.184 GHz) in the young and dense planetary nebula NGC 7027, which is located in the constellation of Cygnus. Very recently, Neufeld et al. (2020) identified the rovibrational transitions ($v = 1$–0 P(1) at 3.51629 μm and $v = 1$–0 P(2) at 3.60776 μm) of HeH^+ in emission. They observed these transitions toward the same planetary nebula NGC 7027 using the iSHELL spectrograph on NASA's Infrared Telescope Facility (IRTF) on Maunakea and confirmed the early discovery reported by Güsten et al. (2019).

Zicler et al. (2017) considered HeH_n^+ clusters in computing the abundances of HeH^+, HeH_2^+ and HeH_3^+ ions. They performed a potential energy surface scan and found HeH_3^+ to be the most favorable cluster to study. They also calculated reaction rate constants for the formation of the HeH_3^+ ion using two different reaction channels. Priestley et al. (2017) performed chemical modeling by considering various Ar- and He-related ions. They predicted HeH^+ emission above detection thresholds. They also pointed out that the formation timescale for this molecule is much longer than the age of the Crab.

Our present paper attempts to model the chemistry of various hydride and hydroxyl cations of argon (ArH^+ and $ArOH^+$), neon (NeH^+ and $NeOH^+$), and helium (HeH^+ and $HeOH^+$) along with their various isotopologs (^{36}Ar, ^{38}Ar, ^{40}Ar, ^{20}Ne, and ^{22}Ne) for conditions in the Crab environment and to find out a favorable parameter space that can explain the observational features. In Section 2, we discuss the adopted physical conditions. In Section 3, a detailed discussion on the adopted chemical pathways and their rates are presented. The chemical modeling results are discussed in Section 4, and finally, in Section 5, we present our concluding remarks.

2. Physical Conditions

Because physical and chemical processes are interrelated, it is essential to use suitable physical conditions to constrain the chemical abundances of the noble gas species considered in this work. Here, we modeled a single Crab Nebula filament by using the Cloudy code (version 17.02, last described by Ferland et al. 2017). Cloudy is a spectral synthesis code that is designed to simulate matter under a broad range of interstellar conditions. It is provided for general use under an open-source license, https://www.nublado.org. Here, we have constructed two models, Model A and Model B, to explain the various aspects of the Crab.

Earlier, Owen & Barlow (2015) modeled the properties of dust and gas densities by fitting the predicted spectral energy distribution (SED) to the multiwavelength observations. Based on their results, here, we used amorphous carbon grain to mimic the dust inside the Crab. For the amorphous carbon grain model, we used the optical constants from Zubko et al. (1996) and adopted a mass density of $1.85\,\mathrm{g\,cm}^{-3}$. We modified the default grain size distribution of Cloudy and assumed that it will maintain a power-law distribution, $n(a) \propto a^{-\alpha}$, with $\alpha = 2.7$, $a_{\mathrm{min}} = 0.005\ \mu$m, and $a_{\mathrm{max}} = 0.5\ \mu$m following the clumpy model VI of Owen & Barlow (2015). We used a higher dust-to-gas mass ratio ($M_d/M_g = 0.027$; Owen & Barlow 2015) suitable for the Crab. In the Cloudy code, the extinction-to-gas ratio $A_V/N(\mathrm{H})$ is self consistently calculated based on the dust-to-gas mass ratio. We obtained an extinction-to-gas ratio of $A_V/N(\mathrm{H}) \sim 2.094 \times 10^{-20}\,\mathrm{mag\,cm}^2$. Priestley et al. (2017) used a similar dust-to-gas mass ratio in their model, but they kept their extinction-to-gas ratio $A_V/N(\mathrm{H})$ at the standard interstellar value ($6.289 \times 10^{-22}\,\mathrm{mag\,cm}^2$), which is about two orders of magnitude lower than the (more realistic) value used here. We assumed that our object is located 2.5 pc away from the central source (i.e., inner radius, $r_{\mathrm{in}} = 2.5$ pc) and the thickness (dr) of our shell is 3.5×10^{16} cm (Priestley et al. 2017). Because we considered $r_{\mathrm{in}} \gg dr$, in principle, a plane-parallel geometry can be assumed. We included the extensive

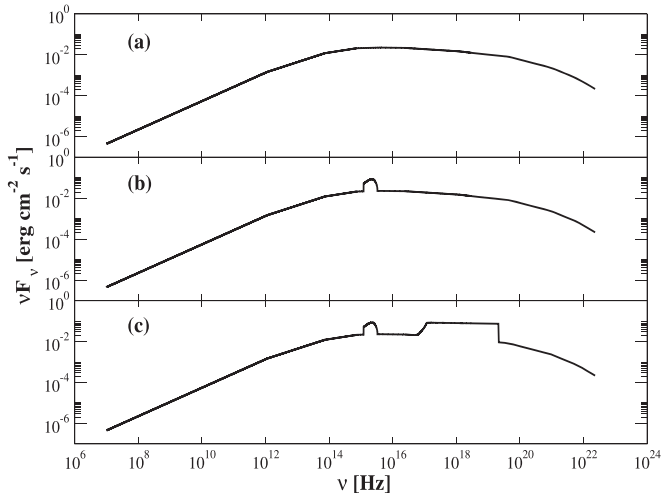

Figure 1. Shape and intensity of the resulting incident SED. The three panels of this figure show the modifications of the SED sequentially. The SED obtained from Hester (2008) is shown in panel (a), panel (b) shows the SED after the inclusion of the Galactic background radiation field of 31 Draine units, and finally, panel (c) shows the resulting complete SED after the inclusion of the X-ray spectrum from Figure 1 of Priestley et al. (2017).

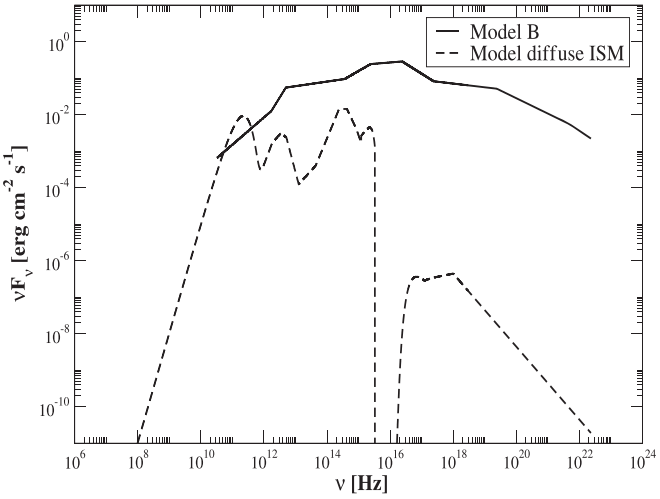

Figure 2. Shape and intensity of the incident SED (Davidson & Fesen 1985) considered for model B are shown with the solid line. The incident SED considered for the diffuse ISM case is shown with the dashed line.

model of the H_2 molecule described by Shaw et al. (2005) in our model calculations. We considered a detailed treatment of the physics of polycyclic aromatic hydrocarbons (PAHs), including photoelectric heating and collisional processes.

We adopted the SED shape mentioned in Hester (2008) and considered the luminosity (L) of the central object to be 1.3×10^{38} erg s^{-1}. Because our object is located 2.5 pc away from the central source, the intensity of the external radiation field striking a unit surface area of the cloud ($L/4\pi r_{\rm in}^2$) is ∼0.174 erg cm^{-2} s^{-1}. The obtained shape and intensity of the SED are shown in Figure 1(a). The Galactic background radiation field proposed by Bertoldi & Draine (1996) is also included to modify our SED. This radiation field is only defined over a narrow wavelength range. The strength of this radiation field was 31 Draine units (i.e., 31× the interstellar radiation field in Draine's units ≈$31 \times 2.7 \times 10^{-3}$ erg s^{-1} cm^{-2}; Draine 1978). The resulting SED with the Galactic background radiation field included is shown in Figure 1(b). We digitally extracted (using https://apps.automeris.io/wpd/) the output X-ray spectrum (i.e., Figure 1) of Priestley et al. (2017) and included an X-ray flux of 0.35 erg cm^{-2} s^{-1} from 0.1 to 100 Å in our SED (Figure 1(c)). The shape and intensity of the final SED used in the case of the Crab is shown in Figure 1(c). All of the parameters discussed here are considered as the input physical parameters of our Model A.

Richardson et al. (2013) studied the nature of the H_2-emitting gas in knot 51 of the Crab. They mentioned that Davidson's SED (Davidson & Fesen 1985) is a reasonable fit to reproduce observations. In Figure 2, we show the SED of Davidson & Fesen (1985; solid curve) for modeling the ionizing particle model following Richardson et al. (2013; Model B). Additionally, we have considered the SED shown in Figure 2 for the diffuse ISM case (dashed curve). Details about this SED and modeling results are discussed in Section 4.1.

All of the relevant physical properties considered here are summarized in Table 1 and the gas-phase elemental abundances are listed in Table 2. Tables 1 and 2 contain input parameters for the two models, Model A and Model B. In Model A, we have considered the physical parameters from Priestley et al. (2017)

Table 1
Adopted Physical Parameters for the Crab Filament

Physical Parameters	Adopted Values
Model A (adopted from Priestley et al. 2017)	
Inner radius ($r_{\rm in}$)	2.5 pc = 7.715×10^{18} cm
Shell thickness (dr)	3.5×10^{16} cm
Luminosity (L)	1.3×10^{38} erg s^{-1}
ISRF	31 Draine units
SED	Hester (2008) + X-ray from Figure 1 of Priestley et al. (2017)
Type of grain	Amorphous carbon
Dust-to-gas mass ratio	0.027 (Owen & Barlow 2015)
Model B (adopted from Richardson et al. 2013)	
Incident ionizing photon flux on the slab (Φ(H))	$10^{10.06}$ cm^{-2} s^{-1}
Thickness	$10^{16.5}$ cm
Additional heating	$\zeta_H/\zeta_0 = 10^{5.3}$
$n_{\rm H(min)}$	10^3 cm^{-3}
$n_{\rm H(core)}$	$10^{5.25}$ cm^{-3}
SED	Davidson & Fesen (1985)
Type of grain	Mix of graphite and silicate
Dust-to-gas mass ratio	0.003

and initial elemental abundances from the clumpy model VI of Owen & Barlow (2015). In Model B, we have considered the initial elemental abundances and physical input parameters for the ionizing particle model that were considered by Richardson et al. (2013) to explain the nature of H_2-emitting gas in the Crab knot 51 filamentary region. Some major differences between the physical parameters of Model A and Model B is that Model A is a constant-density model whereas in Model B, we have considered a dense core ($n_{\rm H(core)} \sim 10^{5.25}$ cm^{-3}) by introducing a varying density profile, and the grain type in both the models is different. The results obtained with Model B are reported in Appendix C. For the initial isotopic ratio of argon and neon, we used ^{36}Ar/^{38}Ar/^{40}Ar = 84.5946/15.3808/0.0246 and ^{20}Ne/^{21}Ne/^{22}Ne = 92.9431/0.2228/6.8341, following Wieler (2002).

Table 2
Initial Gas-phase Elemental Abundances with Respect to Total Hydrogen Nuclei in All Forms for the Crab Filament

Element	Abundance	Element	Abundance
Model A (adopted from Owen & Barlow 2015)			
H	1.00	^{36}Ar	1.00×10^{-5}
He	1.85	^{38}Ar	1.82×10^{-6}
C	1.02×10^{-2}	^{40}Ar	2.90×10^{-9}
N	2.50×10^{-4}	^{20}Ne	4.90×10^{-3}
O	6.20×10^{-3}	^{22}Ne	3.60×10^{-4}
Model B (adopted from Richardson et al. 2013)			
H	1.00	Si	8.91×10^{-6}
He	2.95×10^{-1}	S	1.95×10^{-5}
C	3.98×10^{-4}	Cl	4.68×10^{-8}
N	5.62×10^{-5}	^{36}Ar	4.79×10^{-6}
O	5.25×10^{-4}	^{38}Ar	8.70×10^{-7}
^{20}Ne	1.82×10^{-4}	^{40}Ar	1.39×10^{-9}
^{22}Ne	1.34×10^{-5}	Fe	2.45×10^{-5}
Mg	2.00×10^{-5}		

Note. For the initial isotopic ratio of argon and neon, we have used $^{36}Ar/^{38}Ar/^{40}Ar = 84.5946/15.3808/0.0246$ and $^{20}Ne/^{21}Ne/^{22}Ne = 92.9431/0.2228/6.8341$, following Wieler (2002).

2.1. Radiative Transfer Model

The $J = 1$ and $J = 2$ levels of $^{36}ArH^+$ are at 29.6 K and 88.9 K, respectively. The measured electron temperature (7500–15000 K; Davidson & Fesen 1985) for the ionized gas and measured excitation temperature of H_2 (2000–3000 K; Loh et al. 2011) in the Crab region is much higher than that at these energy levels. If the region where ArH^+ transitions were observed has the density of the colliding partner exceeding the critical density and temperature >100 K, the level populations would be in Boltzmann equilibrium and yield a 2–1/1–0 ratio of ∼30. Because the observed ratio is ∼2, it is expected that the density of the colliding partner is much lower than their critical densities. Barlow et al. (2013) also attributed this difference to the density of the collisional partners being below the critical density of the ArH^+ rotational levels. They used a radiative transfer model to find out the densities of H_2 and e^- from the observational ratio. They obtained a critical density of electrons of $\sim 10^4\ cm^{-3}$ and $H_2 \sim 10^8\ cm^{-3}$.

ArH^+ favors regions where H_2/H is small. If there are any significant H_2 densities, then the reactive collision with ArH^+ may be high enough to affect the excitation. By including the reactive collision rate with H_2, it might be possible to compare between models and observed fluxes to place a limit on the H_2/H ratio in the emitting region. However, with the public version of RADEX, it is not possible to include this feature. Moreover, around the region where ArH^+ was identified in the Crab, the abundance of H atoms and electrons is $>10^4$–10^5 times higher than that of H_2 (see Figure 16 of Priestley et al. 2017 and Figures 9 and C3 in the latter part of this paper). This suggests that a nonreactive collision might be the primary source of excitation of ArH^+ in the Crab filamentary region.

Barlow et al. (2013) used the MADEX code (Cernicharo 2012), where they used H_2 and electron as the collision partner. Due to the unavailability of the collisional rate parameters, they used the collisional deexcitation rate of $SiH^+ + He$ and $CH^+ + e^-$ in place of the interaction of H_2 and e^- with ArH^+, respectively. Because the electron-impact rate coefficient for the dipolar transitions is roughly 10^4–10^5 times larger than the neutrals (H and H_2), Hamilton et al. (2016) used electrons as the only colliding partner. Because reactive collisions are not implemented in the public version of RADEX, we only took the nonreactive collisions into account. We assumed that due to the low abundance of H_2 in the region of ArH^+ formation and high electron-impact rate, reactive collision with H_2 will have minimal effect in this condition. Here, we consider three colliders, H, H_2, and electrons, in RADEX. Collisional rates with H and H_2 are scaled (Schöier et al. 2005) from the available collisional rates of $ArH^+ - He$ obtained from García-Vázquez et al. (2019), and collisional rates with electrons are taken from Hamilton et al. (2016).

Here, we used the RADEX code (van der Tak et al. 2007) for non-LTE computation to explain the observational results. We prepared this collisional data file by using the spectroscopic parameters available in the JPL (Pickett 1991) or CDMS (Müller et al. 2001, 2005) database and included the electron-impact excitation rates from Hamilton et al. (2016). Collisional data files for the other hydride/hydroxyl cations were mostly unavailable in the Cloudy code as well. We used our approximated data files for the calculation of the surface brightness/emissivity discussed in the later part of this manuscript. We considered Figure 1(c) as the input of the background radiation field in the radiative transfer calculations reported here. We prepared the self-made background radiation field in the format prescribed in https://personal.sron.nl/~vdtak/radex/index.shtml. This file contains three columns. The first column is the wavenumber (cm^{-1}), the second is the intensity (in units of $Jy\ nsr^{-1}$), and the third is the dilution factor. The dilution factor varies between 0 and 1. Here, for the estimation, we used an average dilution factor of 0.5. We did not find a significant difference while considering a different dilution factor in our calculations.

We have drawn a parameter space with a wide range of H densities (1–10^8 cm^{-3}), H_2 densities (10^{-2}–$10^4\ cm^{-3}$), electron number densities (1–$10^6\ cm^{-3}$), and excitation temperatures (10–3000 K). Figure 3 shows the surface brightness ratio between the $2 \rightarrow 1$ and $1 \rightarrow 0$ transitions of $^{36}ArH^+$. For this computation, we considered the column density of $^{36}ArH^+ \sim 1.7 \times 10^{12}\ cm^{-2}$ as obtained from Hamilton et al. (2016) and a line width (FWHM) of $5\ km\ s^{-1}$. For the left four panels, we considered the H_2 density of $1\ cm^{-3}$ and temperature fixed at 10 K, 100 K, 1000 K, and 3000 K, respectively. Some contours near the observed surface brightness ratio (∼2) are highlighted in all the panels. The top-left panel of Figure 3 shows that at 10 K, the surface brightness ratio between these two transitions is ∼0. This is because the excitation temperature is below the upstate energy of these two transitions. For the higher temperature, energy levels are gradually populated and the ratio increases. The left four panels of Figure 3 depict how the observed ratio is obtained with an electron density of 1000–$3000\ cm^{-3}$ when the number density of H atoms is $<10^6$–$10^7\ cm^{-3}$ and the temperature is beyond the upstate energy of $2 \rightarrow 1$ and $1 \rightarrow 0$. For the case with temperature 100 K, when H density is below $\sim 10^7\ cm^{-3}$, the observed ratio is obtained with an electron density $\sim 1000\ cm^{-3}$. For $n_H \sim 10^7\ cm^{-3}$, the observed ratio is obtained with n_e = 1–$1000\ cm^{-3}$. As we gradually increase the temperature, the observed ratio is obtained at a lower H density (for example, at 1000 K, it is a ∼few times $\times 10^6\ cm^{-3}$) and a little higher electron density range (1–$2000\ cm^{-3}$). If the temperature is further increased from here (i.e., at 3000 K), a very small decrease of n_H and a little increase

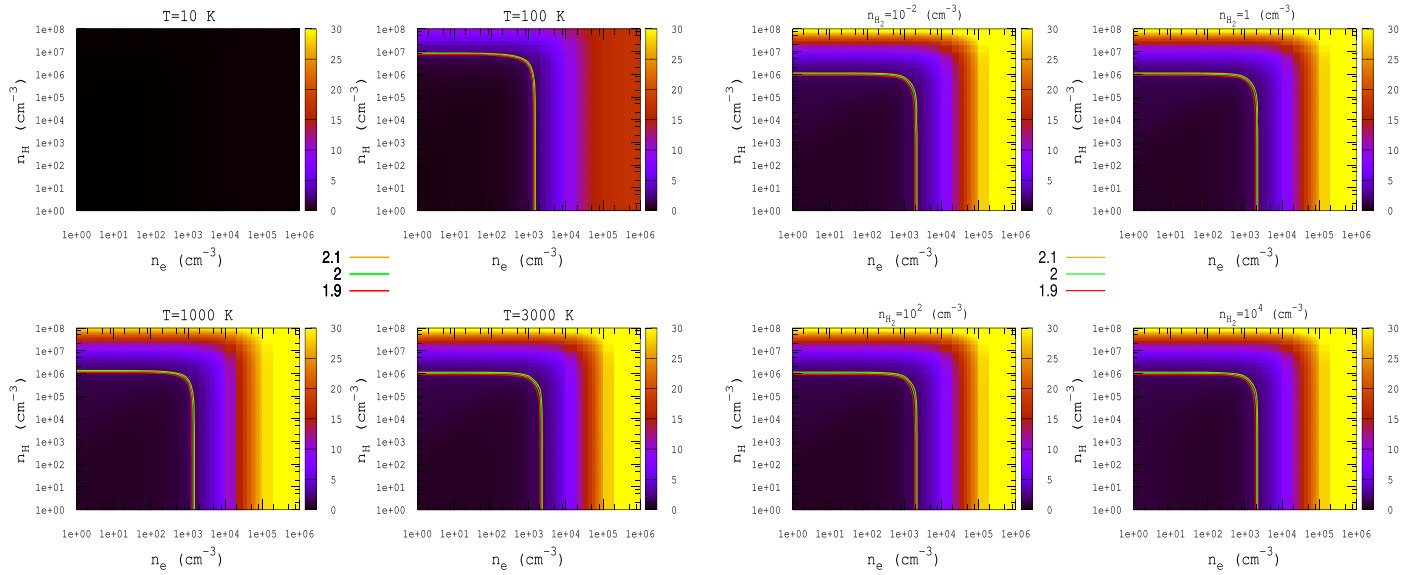

Figure 3. Surface brightness (SB) ratio between the 2−1 and 1−0 transitions of $^{36}ArH^+$ by considering a column density of 1.7×10^{12} cm^{-2}. The left four panels show the cases with fixed temperatures (T = 10, 100, 1000, and 3000 K, respectively) whereas the right four panels show the cases with fixed H_2 density ($n_{H_2} = 10^{-2}$, 1, 10^2, and 10^4 cm^{-3}, respectively). The contours are highlighted near the observed SB ratio (of ∼2).

in n_e range are required to reproduce the observed ratio. For the higher temperature (∼3000 K) and higher electron density (>10^5), the highest value of the ratio, ∼30, is achieved. This value is also obtained when the H density is around 10^8 cm^{-3}. Thus, the critical density of electrons and hydrogen atoms is 10^5 cm^{-3} and 10^8 cm^{-3} respectively. In the right four panels of Figure 3, we kept the temperature fixed at 2700 K and the H_2 density fixed at 10^{-2} cm^{-3}, 1 cm^{-3}, 10^2 cm^{-3}, and 10^4 cm^{-3} respectively. All four panels give a similar result, which implies that the excitation is independent of the H_2 collision. The left four panels of Figure 3 remain unchanged when H_2 is omitted as a collider. The right four panels show that it is independent of the collision of H_2 when the H_2 density is <10^4 cm^{-3}. However, the reactive collisions with H_2 may show differences that are not considered here due to the limitations of the public version of the RADEX code. In brief, we found that it is only the nonreactive collision with electrons that can successfully explain the excitation of ArH^+ when the temperature is beyond the upstate energy of these two levels discussed here. Loh et al. (2012) estimated the electron number density and total hydrogen number density ($n(H^+) + n(H) + 2n(H_2)$) in the filaments and knots to be around 1400–2500 cm^{-3} and 14,000–25,000 cm^{-3} respectively. Barlow et al. (2013) estimated the electron number density of a ∼few times 100 cm^{-3}. Our results shown in the left four panels of Figure 3 require an n_e of ∼2000–3000 cm^{-3} to reproduce the observed ratio around the measured excitation temperature of H_2. Only the nonreactive collision with electrons can explain the ArH^+ excitation in the crab.

3. Chemical Pathways

Following the reaction network of ArH^+ presented in Priestley et al. (2017), here, we prepared similar pathways for the formation and destruction of NeH^+ and HeH^+. Additionally, we prepared the pathways for the formation and destruction of the hydroxyl cations of these noble gas species ($ArOH^+$, $NeOH^+$, and $HeOH^+$) under similar environments. In Table 3, we have listed the reaction network adopted here to study the chemical evolution of the related hydride and hydroxyl cations along with the corresponding rate coefficients used. The enlisted rate coefficients are either estimated or taken from the literature as mentioned in the footnote. In the following subsections, we present an extensive discussion for the preparation or adaptation of the rate coefficients of the various kinds of reactions considered. We used the reaction rates of UMIST as the default for the other reactions. For H_2 formation on grains, we have used the modified "Jura rate" (Sternberg & Neufeld 1999) for Model A. The default "Jura rate" of H_2 formation is 3×10^{-17} cm^3 s^{-1} (Jura 1975). In the case of Model B, the chemical pathways are the same as discussed above, except the H_2 formation rate is through grain catalysis. This rate is taken from Cazaux & Tielens (2002) as it was considered by Richardson et al. (2013).

3.1. Cosmic-Ray Ionization Rate

The cosmic-ray ionization rate affects the chemical and ionization state of the gas. The Cloudy code was developed to deal with various astrophysical environments. This code actually deals with the cosmic-ray density. It automatically converts the given cosmic-ray ionization rates into the cosmic-ray density internally. It considers the cosmic-ray ionization rate to be 2×10^{-16} s^{-1} per H (ζ'_H) and 4.6×10^{-16} s^{-1} per H_2 (ζ'_{H_2}) by default. Thus, the default rate per H_2 (ζ'_{H_2}) is 2.3 times higher than that of H ($\zeta_H{}'$). The factor 2.3 instead of 2 in the relation arises due to the contribution of the ionization produced by the secondary ionizations by suprathermal electrons knocked off in the primary ionization. Here, we used the cosmic-ray ionization rate per H_2 as $\zeta_{H_2} = \zeta_0 = 1.3 \times 10^{-17}$ s^{-1} (Cloudy code scales it with respect to ζ'_H to consider the cosmic-ray density) as our standard rate and varied the rate (in between ζ_0 and $10^8\zeta_0$) with respect to it. This means our standard $\zeta_H = 5.65 \times 10^{-18}$ s^{-1}. In Table 3, reaction number 1 (CR) of the Ar chemistry represents the cosmic-ray ionization rate by ζ_H and reaction number 2 (CRPHOT) by ζ_{H_2}. For similar cosmic-ray ionization reactions with He and Ne chemistry, we considered the same leading coefficient as used for Ar chemistry in Schilke et al. (2014) and

Table 3
Reaction Pathways for the Formation and Destruction of Some Noble Gas Ions

Reaction Number (Type)	Reactions	Rate Coefficient	References and Comments
	Ar chemistry		
1 (CR)	$Ar + CR \rightarrow Ar^+ + e^-$	$10\zeta_{H,cr}$ s^{-1}	a, d
2 (CRPHOT)	$Ar + CRPHOT \rightarrow Ar^+ + e^-$	$0.8\frac{\zeta_{H_2,cr}}{1-\omega}$ s^{-1}	a, d
3 (IN)	$Ar + H_2^+ \rightarrow ArH^+ + H$	10^{-9} cm^3 s^{-1}	a
4 (IN)	$Ar + H_3^+ \rightarrow ArH^+ + H_2$	$8 \times 10^{-10}\exp\left(\frac{-6019\ K}{T}\right)$ cm^3 s^{-1}	This work
5 (IN)	$Ar^+ + H_2 \rightarrow ArH^+ + H$	$8.4 \times 10^{-10}\left(\frac{T}{300\ K}\right)^{0.16}$ cm^3 s^{-1}	a
6 (IN)	$ArH^+ + H_2 \rightarrow Ar + H_3^+$	8×10^{-10} cm^3 s^{-1}	a
7 (IN)	$ArH^+ + CO \rightarrow Ar + HCO^+$	1.25×10^{-9} cm^3 s^{-1}	a
8 (IN)	$ArH^+ + O \rightarrow Ar + OH^+$	8×10^{-10} cm^3 s^{-1}	a
9 (IN)	$ArH^+ + C \rightarrow Ar + CH^+$	8×10^{-10} cm^3 s^{-1}	a
10 (IN)	$Ar^{++} + H \rightarrow Ar^+ + H^+$	10^{-15} cm^3 s^{-1}	b
11 (RA)	$Ar + OH^+ \rightarrow ArOH^+ + h\nu$	1.9×10^{-17} cm^3 s^{-1}	c, m
12 (RA)	$Ar^+ + OH \rightarrow ArOH^+ + h\nu$	1.5×10^{-17} cm^3 s^{-1}	c, m
13 (RA)	$ArH^+ + O \rightarrow ArOH^+ + h\nu$	3.0×10^{-17} cm^3 s^{-1}	c, m
14 (IN)	$Ar + N_2^+ \rightarrow Ar^+ + N_2$	3.65×10^{-10} cm^3 s^{-1}	d
15 (IN)	$Ar^+ + H_2 \rightarrow Ar + H_2^+$	2.00×10^{-12} cm^3 s^{-1}	d
16 (IN)	$Ar^+ + O_2 \rightarrow Ar + O_2^+$	3.50×10^{-11} cm^3 s^{-1}	d
17 (IN)	$Ar^+ + CH_4 \rightarrow CH_2^+ + Ar + H_2$	1.40×10^{-10} cm^3 s^{-1}	d
18 (IN)	$Ar^+ + CH_4 \rightarrow CH_3^+ + Ar + H$	7.90×10^{-10} cm^3 s^{-1}	d
19 (IN)	$Ar^+ + HCl \rightarrow Ar + HCl^+$	2.90×10^{-10} cm^3 s^{-1}	d
20 (IN)	$Ar^+ + HCl \rightarrow ArH^+ + Cl$	6.00×10^{-11} cm^3 s^{-1}	d
21 (IN)	$Ar^+ + CO \rightarrow Ar + CO^+$	2.80×10^{-11} cm^3 s^{-1}	d
22 (IN)	$Ar^+ + NH_3 \rightarrow Ar + NH_3^+$	1.60×10^{-9} cm^3 s^{-1}	d
23 (IN)	$Ar^+ + N_2 \rightarrow Ar + N_2^+$	1.20×10^{-11} cm^3 s^{-1}	d
24 (IN)	$Ar^+ + H_2O \rightarrow Ar + H_2O^+$	1.30×10^{-9} cm^3 s^{-1}	d
25 (XR)	$Ar + XR \rightarrow Ar^{++} + e^- + e^-$	ζ_{XR} s^{-1}	d, e
26 (XR)	$Ar^+ + XR \rightarrow Ar^{++} + e^-$	ζ_{XR} s^{-1}	d, e
27 (XRSEC)	$Ar + XRSEC \rightarrow Ar^+ + e^-$	$5.53\zeta_{H,XRPHOT}$ s^{-1}	d, l
28 (XRPHOT)	$Ar + XRPHOT \rightarrow Ar^+ + e^-$	$0.8\frac{\zeta_{H2,XRPHOT}}{1-\omega}$ s^{-1}	d, l
29 (ER)	$Ar^+ + e^- \rightarrow Ar + h\nu$	...	d
30 (ER)	$Ar^{++} + e^- \rightarrow Ar^+ + h\nu$	...	d
31 (DR)	$ArH^+ + e^- \rightarrow Ar + H$	10^{-11} cm^3 s^{-1}	a, k
32 (DR)	$ArOH^+ + e^- \rightarrow Ar + OH$	10^{-11} cm^3 s^{-1}	This work
33 (PH)	$ArH^+ + h\nu \rightarrow Ar^+ + H$	$4.20 \times 10^{-12}\exp(-3.27A_v)$ s^{-1}	h
34 (PH)	$ArOH^+ + h\nu \rightarrow Ar + OH^+$	$4.20 \times 10^{-12}\exp(-3.27A_v)$ s^{-1}	This work
	Ne chemistry		
1 (CR)	$Ne + CR \rightarrow Ne^+ + e^-$	$10\zeta_{H,cr}$ s^{-1}	This work, d
2 (CRPHOT)	$Ne + CRPHOT \rightarrow Ne^+ + e^-$	$0.8\frac{\zeta_{H_2,cr}}{1-\omega}$ s^{-1}	This work, d
3 (IN)	$Ne + H_2^+ \rightarrow NeH^+ + H$	$2.58 \times 10^{-10}\exp\left(\frac{-6717\ K}{T}\right)$ cm^3 s^{-1}	This work
4 (IN)	$Ne + H_3^+ \rightarrow NeH^+ + H_2$	$8 \times 10^{-10}\exp\left(\frac{-27456\ K}{T}\right)$ cm^3 s^{-1}	This work
5a (IN)	$Ne^+ + H_2 \rightarrow NeH^+ + H$	$3.2 \times 10^{-9}\left(\frac{T}{300\ K}\right)^{0.16}$ cm^3 s^{-1}	This work
5b (IN)	$Ne^+ + H_2 \rightarrow Ne + H + H^+$	$1.98 \times 10^{-14}\exp(-35\ K/T)$ cm^3 s^{-1}	This work
5c (IN)	$Ne^+ + H_2 \rightarrow Ne + H_2^+$	4.84×10^{-15} cm^3 s^{-1}	This work
6 (IN)	$NeH^+ + H_2 \rightarrow Ne + H_3^+$	3.65×10^{-9} cm^3 s^{-1}	This work
7 (IN)	$NeH^+ + CO \rightarrow Ne + HCO^+$	2.26×10^{-9} cm^3 s^{-1}	This work
8 (IN)	$NeH^+ + O \rightarrow Ne + OH^+$	2.54×10^{-9} cm^3 s^{-1}	This work
9 (IN)	$NeH^+ + C \rightarrow Ne + CH^+$	1.15×10^{-9} cm^3 s^{-1}	This work
10 (IN)	$Ne^{++} + H \rightarrow Ne^+ + H^+$	1.94×10^{-15} cm^3 s^{-1}	This work
11 (RA)	$Ne + OH^+ \rightarrow NeOH^+ + h\nu$	1.4×10^{-18} cm^3 s^{-1}	c, m
12 (RA)	$Ne^+ + OH \rightarrow NeOH^+ + h\nu$	7.5×10^{-17} cm^3 s^{-1}	c, m
13 (RA)	$NeH^+ + O \rightarrow NeOH^+ + h\nu$	2.3×10^{-17} cm^3 s^{-1}	c, m
14 (IN)	$HeH^+ + Ne \rightarrow NeH^+ + He$	1.25×10^{-9} cm^3 s^{-1}	d
15 (IN)	$NeH^+ + He \rightarrow HeH^+ + Ne$	3.8×10^{-14} cm^3 s^{-1}	d
16 (IN)	$Ne^+ + CH_4 \rightarrow CH^+ + Ne + H_2 + H$	8.4×10^{-13} cm^3 s^{-1}	d

Table 3
(Continued)

Reaction Number (Type)	Reactions	Rate Coefficient	References and Comments
17 (IN)	$Ne^+ + CH_4 \rightarrow CH_2^+ + Ne + H_2$	4.2×10^{-12} cm^3 s^{-1}	d
18 (IN)	$Ne^+ + CH_4 \rightarrow CH_3^+ + Ne + H$	4.7×10^{-12} cm^3 s^{-1}	d
19 (IN)	$Ne^+ + CH_4 \rightarrow CH_4^+ + Ne$	1.1×10^{-11} cm^3 s^{-1}	d
20 (IN)	$Ne^+ + NH_3 \rightarrow NH^+ + Ne + H_2$	4.5×10^{-12} cm^3 s^{-1}	d
21 (IN)	$Ne^+ + NH_3 \rightarrow NH_2^+ + Ne + H$	1.9×10^{-10} cm^3 s^{-1}	d
22 (IN)	$Ne^+ + NH_3 \rightarrow NH_3^+ + Ne$	2.7×10^{-11} cm^3 s^{-1}	d
23 (IN)	$Ne^+ + N_2 \rightarrow N_2^+ + Ne$	1.1×10^{-13} cm^3 s^{-1}	d
24 (IN)	$Ne^+ + H_2O \rightarrow H_2O^+ + Ne$	8.0×10^{-10} cm^3 s^{-1}	d
25 (IN)	$Ne^+ + O_2 \rightarrow O^+ + Ne + O$	6.0×10^{-11} cm^3 s^{-1}	d
26 (XR)	$Ne + XR \rightarrow Ne^{++} + e^- + e^-$	ζ_{XR} s^{-1}	d, e
27 (XR)	$Ne^+ + XR \rightarrow Ne^{++} + e^-$	ζ_{XR} s^{-1}	d, e
28 (XRSEC)	$Ne + XRSEC \rightarrow Ne^+ + e^-$	$1.84\zeta_{H,XRPHOT}$ s^{-1}	d, l
29 (XRPHOT)	$Ne + XRPHOT \rightarrow Ne^+ + e^-$	$0.8\frac{\zeta_{H2,XRPHOT}}{1-\omega}$ s^{-1}	d, l
30 (ER)	$Ne^+ + e^- \rightarrow Ne + h\nu$	...	d
31 (ER)	$Ne^{++} + e^- \rightarrow Ne^+ + h\nu$	...	d
32 (DR)	$NeH^+ + e^- \rightarrow Ne + H$	10^{-11} cm^3 s^{-1}	This work
33 (DR)	$NeOH^+ + e^- \rightarrow Ne + OH$	10^{-11} cm^3 s^{-1}	This work
34 (PH)	$NeH^+ + h\nu \rightarrow Ne^+ + H$	$4.20 \times 10^{-12}\exp(-3.27A_v)$ s^{-1}	This work
35 (PH)	$NeOH^+ + h\nu \rightarrow Ne + OH^+$	$4.20 \times 10^{-12}\exp(-3.27A_v)$ s^{-1}	This work
	He chemistry		
1 (CR)	$He + CR \rightarrow He^+ + e^-$	$10\zeta_{H,cr}$ s^{-1}	This work, d
2 (CRPHOT)	$He + CRPHOT \rightarrow He^+ + e^-$	$0.8\frac{\zeta_{H2,cr}}{1-\omega}$ s^{-1}	This work, d
3 (IN)	$He + H_2^+ \rightarrow HeH^+ + H$	$3 \times 10^{-10}\exp\left(\frac{-6717\ K}{T}\right)$ cm^3 s^{-1}	n
4 (IN)	$He + H_3^+ \rightarrow HeH^+ + H_2$	$8 \times 10^{-10}\exp\left(\frac{-29110\ K}{T}\right)$ cm^3 s^{-1}	This work
5a (IN)	$He^+ + H_2 \rightarrow HeH^+ + H$	...	Not considered
5b (IN)	$He^+ + H_2 \rightarrow He + H + H^+$	$3.70 \times 10^{-14}\exp(-35\ K/T)$ cm^3 s^{-1}	This work, UMIST
5c (IN)	$He^+ + H_2 \rightarrow He + H_2^+$	7.20×10^{-15} cm^3 s^{-1}	This work, UMIST
6 (IN)	$HeH^+ + H_2 \rightarrow He + H_3^+$	1.26×10^{-9} cm^3 s^{-1}	j
7 (IN)	$HeH^+ + CO \rightarrow He + HCO^+$	2.33×10^{-9} cm^3 s^{-1}	This work
8 (IN)	$HeH^+ + O \rightarrow He + OH^+$	2.68×10^{-9} cm^3 s^{-1}	This work
9 (IN)	$HeH^+ + C \rightarrow He + CH^+$	1.18×10^{-9} cm^3 s^{-1}	This work
10 (IN)	$He^{++} + H \rightarrow He^+ + H^+$	2.45×10^{-15} cm^3 s^{-1}	This work
11 (RA)	$He + OH^+ \rightarrow HeOH^+ + h\nu$	2.2×10^{-18} cm^3 s^{-1}	c, m
12 (RA)	$He^+ + OH \rightarrow HeOH^+ + h\nu$	1.7×10^{-16} cm^3 s^{-1}	c, m
13 (RA)	$HeH^+ + O \rightarrow HeOH^+ + h\nu$	2.8×10^{-17} cm^3 s^{-1}	c, m
14 (IN)	$HeH^+ + H \rightarrow He + H_2^+$	1.7×10^{-9} cm^3 s^{-1}	n
15 (RA)	$He^+ + H \rightarrow HeH^+ + h\nu$	1.44×10^{-16} cm^3 s^{-1}	i, n
16 (RA)	$He + H^+ \rightarrow HeH^+ + h\nu$	$5.6 \times 10^{-21}\left(\frac{T}{10^4\ K}\right)^{-1.25}$ cm^3 s^{-1}	d, n
17 (XR)	$He + XR \rightarrow He^{++} + e^- + e^-$	ζ_{XR} s^{-1}	d, e
18 (XR)	$He^+ + XR \rightarrow He^{++} + e^-$	ζ_{XR} s^{-1}	d, e
19 (XRSEC)	$He + XRSEC \rightarrow He^+ + e^-$	$0.84\zeta_{H,XRPHOT}$ s^{-1}	d, l
20 (XRPHOT)	$He + XRPHOT \rightarrow He^+ + e^-$	$0.8\frac{\zeta_{H2,XRPHOT}}{1-\omega}$ s^{-1}	d, l
21 (ER)	$He^+ + e^- \rightarrow He + h\nu$	...	d
22 (ER)	$He^{++} + e^- \rightarrow He^+ + h\nu$	...	d
23 (DR)	$HeH^+ + e^- \rightarrow He + H$	$4.3 \times 10^{-10}\left(\frac{T}{10^4\ K}\right)^{-0.5}$ cm^3 s^{-1}	n
24 (DR)	$HeOH^+ + e^- \rightarrow He + OH$	$4.3 \times 10^{-10}\left(\frac{T}{10^4\ K}\right)^{-0.5}$ cm^3 s^{-1}	This work
25 (PH)	$HeH^+ + h\nu \rightarrow He^+ + H$	...	d, n
26 (PH)	$HeOH^+ + h\nu \rightarrow He + OH^+$	$4.20 \times 10^{-12}\exp(-3.27A_v)$ s^{-1}	This work
27	$He^+ + H^- \rightarrow HeH^+ + e^-$	$3.2 \times 10^{-11}\left(\frac{T}{10^4\ K}\right)^{-0.34}$ cm^3 s^{-1}	n
	Additional modified chemistry		
1 (RA)	$H^+ + H \rightarrow H_2^+ + h\nu$	$2.3 \times 10^{-16}\left(\frac{T}{10^4\ K}\right)^{1.5}$ cm^3 s^{-1}	d, n

Table 3
(Continued)

Reaction Number (Type)	Reactions	Rate Coefficient	References and Comments
2 (DR)	$H_2^+ + e^- \rightarrow H + H$	$3 \times 10^{-9}\left(\frac{T}{10^4\ \mathrm{K}}\right)^{-0.4}$ cm^3 s^{-1}	d, n
3 (IN)	$H_2^+ + H \rightarrow H_2 + H^+$	6.4×10^{-10} cm^3 s^{-1}	d, n

Notes. CR refers to cosmic rays, CRPHOT to secondary photons produced by cosmic rays, XR to direct X-rays, XRSEC to secondary electrons produced by X-rays, XRPHOT to secondary photons from X-rays, IN to ion–neutral reactions, RA to radiative association reactions, ER to electronic recombination reactions for atomic ions, DR to dissociative recombination reactions for molecular ions, PH to photodissociation reactions, $h\nu$ to a photon, ζ to cosmic-ray or X-ray ionization rates, and ω to the dust albedo.
[a] Schilke et al. (2014).
[b] Kingdon & Ferland (1996).
[c] This lower limit of the rate is calculated following Bates (1983), described in Section 3.3.
[d] Reaction pathways are already included or automatically calculated in Cloudy by default.
[e] Meijerink & Spaans (2005).
[h] Roueff et al. (2014).
[i] Güsten et al. (2019).
[j] Orient (1977).
[k] Priestley et al. (2017).
[l] See Appendix A for the calculation details. Here, we are not considering this rate because we are using default values in Cloudy. In the Cloudy code, these values are automatically calculated without any special actions being required.
[m] This upper limit of the rate is of $\sim 10^{-10}$ cm^3 s^{-1}. See Section 3.3 for a more detailed discussion regarding this upper limit.
[n] Neufeld et al. (2020). and references therein.

Priestley et al. (2017). In Cloudy, the direct ionization by cosmic rays is automatically considered for all ionization stages and all elements.

3.2. Ion–Neutral Reaction Rate

The rate coefficients of the ion–neutral (IN) reaction of Ar-related species were already discussed in Priestley et al. (2017). In constructing the reaction network with He and Ne, we either assumed the same rate constants as used for the IN reactions of Ar or used some educated guess. We also included the reaction pathways and rate constants from Güsten et al. (2019), Neufeld et al. (2020), and Orient (1977). In Table 3, the IN rates are given in reaction numbers 3–10, 14–24 for Ar, 3–10, 14–25 for Ne, and 3–10, 14 for He chemistry. Reaction numbers 14–24 of Ar and 14–25 of Ne chemistry were not considered in Priestley et al. (2017). However, these pathways are included in the Cloudy default network, and thus, we used it.

For reaction 3 ($Ar + H_2^+ \rightarrow ArH^+ + H$) of Ar, we considered a rate coefficient of 10^{-9} cm^3 s^{-1} following Priestley et al. (2017). We also used quantum-chemical calculations (DFT B3LYP/6-311++G(d,p) level of theory) with the Gaussian 09 suite of the program (Frisch et al. 2013) and found that this reaction is highly exothermic. Similar calculations for NeH^+ formation ($Ne + H_2^+ \rightarrow NeH^+ + H$) and HeH^+ formation ($He + H_2^+ \rightarrow HeH^+ + H$) show a highly endothermic nature. Neufeld et al. (2020) considered a rate coefficient of $\sim 3 \times 10^{-10} \exp\left(\frac{-6717\ \mathrm{K}}{T}\right)$ cm^3 s^{-1} for the HeH^+ formation by this reaction. We noticed that the endothermicity of NeH^+ formation by this reaction is smaller than that of the endothermicity of HeH^+. Because no reference was available for $Ne + H_2^+ \rightarrow NeH^+ + H$, we scaled the HeH^+ formation rate here and used $\sim 2.58 \times 10^{-10} \exp\left(\frac{-6717\ \mathrm{K}}{T}\right)$ cm^3 s^{-1} in our network.

In the case of reaction 4 ($X + H_3^+ \rightarrow XH^+ + H_2$) of Ar, an endothermic value of about 6400 K was used by Priestley et al. (2017). We used the same empirical relation for the reaction between H_3^+ and He/Ne. From our quantum-chemical calculations, we obtained endothermic values of about 6019 K, 27456 K, and 29110 K for reaction 4 of the Ar-, Ne-, and He-related pathways respectively and used these values for the computation of the rate constant of reaction 4 shown in Table 3.

We calculated the reaction enthalpies for reaction numbers 5–10 of Table 3 and found all reactions are exothermic. The rate constants of some of these reactions for Ar were already given in Priestley et al. (2017), and we used the same. For the estimation of the rate constant for Ne, we derived a scaling factor depending on our computed exothermicity values. Because reaction 5a of the He chemistry network was not considered by the earlier studies (Güsten et al. 2019; Neufeld et al. 2020), we are not considering this reaction here. We considered two other routes of Ne and He chemistry having the possible product channels 5(b) $X^+ + H_2 \rightarrow X + H + H^+$ and 5(c) $X^+ + H_2 \rightarrow X + H_2^+$. In the case of X = Ne, channel 5(b) is considered because the ionization potential of Ne (21.56 eV) is greater than the sum of the ionization potential of H and the dissociation energy of H_2, i.e., (13.60 + 4.48) eV = 18.08 eV. In the UMIST network, we found that similar reaction channels (5b and 5c) were available for the X = He chemistry network. By calculating the reaction enthalpies and comparing them between reactions 5b and 5c of the Ne and He networks, we again obtained scaling factors to estimate the rate coefficients of reactions 5b and 5c of the Ne chemistry network.

For the rate coefficient for the destruction of ArH^+ with H_2, we considered the same one used in Priestley et al. (2017). For the destruction of HeH^+ by H_2 (i.e., reaction number 6 of the He chemistry), we used the rate coefficient measured by Orient (1977). For the NeH^+ destruction by H_2, we used a scaling technique similar to that mentioned earlier. We prepared the IN reaction network of He according to the very recent work by Neufeld et al. (2020). For the sake of completeness, they updated the reaction network developed by Güsten et al. (2019) and added several formation and destruction reactions related

to He. We included the HeH^+ destruction by H (reaction 14 of the He network) with a constant rate coefficient 1.7×10^{-9} cm^3 s^{-1}.

3.3. Radiative Association

Recently, Theis & Fortenberry (2016) studied the formation of $ArOH^+$ and $NeOH^+$ quantum-chemically. They considered three channels for the formation of $NeOH^+$ (by $Ne^+ + OH$, $NeO + H^+$, and $NeH^+ + O$) and three channels for the formation of $ArOH^+$ (by $Ar^+ + OH$, $ArO + H^+$, and $ArH^+ + O$). According to their relative energy calculations, $ArOH^+$ remains in an energy state lower than the total relative energy of their reactants and products (see Figure 2 of Theis & Fortenberry 2016), whereas $NeOH^+$ leads to a likely spontaneous dissociation into Ne and OH^+ (see Figure 1 of Theis & Fortenberry 2016). Because the reactants have higher energy, some energy is released during its formation. These reactions could be treated as radiative association reactions (reaction numbers 11–13 of Table 3). We calculated the rate constant of these reactions by using the method described below (Bates 1983):

$$K = 1 \times 10^{-21} A_r \frac{(6E_0 + N - 2)^{3N-7}}{(3N-7)!} \text{ cm}^3 \text{ s}^{-1}. \quad (1)$$

This temperature-independent semiempirical relation provided by Bates (1983) requires the association energy (E_0) in eV, numbers of nuclei (N) in the complex, and transition probability (A_r) in s^{-1}, which is taken to be 100, as suggested by Bates (1983). The calculated rates for reactions 11–13 are noted in Table 3. But note that this semiempirical relation provided by Bates (1983) is temperature-independent and estimated at ∼30 K. Here, we are dealing with Crab knots, where the temperature is much higher. Keeping this in mind, additionally, we considered an upper limit (10^{-10} cm^3 s^{-1}) to these reactions. Although Theis & Fortenberry (2016) did not consider the reaction between X (=Ar, Ne, and He) and OH^+ for the formation of XOH^+, we considered reaction number 11 of each network because we found it to be exothermic.

We adopted the value of 1.44×10^{-16} cm^3 s^{-1} as the rate coefficient of the HeH^+ formation reaction (He-related reaction number 15, i.e., $He^+ + H \rightarrow HeH^+ + h\nu$). Güsten et al. (2019) ignored $He + H^+ \rightarrow HeH^+ + h\nu$ (reaction 16 of He-related reactions) in the planetary nebula environment, which dominates HeH^+ formation in the early universe. But Neufeld et al. (2020) considered the same formation of HeH^+ through the radiative association reaction using a temperature-dependent rate of $5.6 \times 10^{-21}\left(\frac{T}{10^4 \text{ K}}\right)^{-1.25}$ cm^3 s^{-1}. Here also, we used the same rate coefficient for reaction 16 of the He network.

3.4. X-Ray Ionization Rate

X-ray photoionization, including inner-shell ionization and Auger cascades, collisional ionization by secondary electrons coming from the inner-shell photoionization, are fully treated in Cloudy for all basic elements without any special action being required. However, the physical conditions adopted here demand a chemical network that takes the effect of X-ray ionization into account. We need to consider the three types of X-ray-induced reactions, namely (a) ionization by direct X-rays (ζ_{XR}), (b) secondary ionization by X-rays (ζ_{XRPHOT}), and (c) electron-impact X-ray ionization (ζ_{XRSEC}). The X-ray can mainly ionize the heavy elements by removing the K-shell electron. The vacancy created by the removal of K-shell electron is then filled by Auger transitions. During this process, other electrons and X-ray photons are emitted by the ion, resulting in multiply ionized species. X-ray ionization is a very important means to dictate the chemistry around the Crab environment. Here, we computed various X-ray ionization rates by adopting the method used in Meijerink & Spaans (2005). Though these calculated rates are not directly used in the Cloudy model, it will be very useful to build the noble-gas-related pathways from scratch. Please see Appendix A of this paper for the detailed process of the estimation of the X-ray ionization rate.

3.5. Electronic and Dissociative Recombination

We have considered the electronic recombination (ER) reactions of all the noble gas atomic ions (X^+, X^{++} for X = Ar, Ne, He) and dissociative recombination (DR) reactions of all the noble gas molecular ions (XH^+, XOH^+ for X = Ar, Ne, He). The ER reactions with numbers 29–30 for Ar, 30–31 for Ne, and 21–22 for He are treated automatically in Cloudy to make sure that they correctly balance the inverse photoionization processes, so we did not include them again. We list them in Table 3 for the sake of completeness. Priestley et al. (2017) considered a temperature-dependent rate coefficient for ER of Ar^+ (Schilke et al. 2014) and Ar^{++} (Shull & van Steenberg 1982).

For the DR of ArH^+, Priestley et al. (2017) considered a typical rate of about 10^{-9} cm^3 s^{-1} for their initial model following Schilke et al. (2014) and a reduced rate of 10^{-11} cm^3 s^{-1} for their final models. Abdoulanziz et al. (2018) presented the cross sections for DR and electron-impact vibrational excitation of ArH^+ at electron energies appropriate for the interstellar environment and found very low values of the DR rate coefficients at temperatures below 1000 K, which leads to the conclusion that the collisions with H_2 molecules and the photodissociation are the only significant ArH^+ destruction mechanisms in the ISM. Here, we considered a temperature-independent rate constant of 10^{-11} cm^3 s^{-1}, similar to the final models of Priestley et al. (2017) for the DR of ArH^+. In addition, we assumed that the same rate constant of 10^{-11} is valid for the DR of $ArOH^+$, NeH^+, and $NeOH^+$. For HeH^+, we used the very recently updated temperature-dependent rate of $4.3 \times 10^{-10}(T/10^4 \text{ K})^{-0.5}$ cm^3 s^{-1} following Neufeld et al. (2020). For $HeOH^+$, we considered the same DR rate as it was considered for HeH^+.

3.6. Photodissociation

We have considered the photodissociation (PH) reactions of the hydride and hydroxyl cations. The rate coefficients of these reactions (except the PH reaction of HeH^+; i.e., He chemistry reaction number 25) were considered to be the same as considered for the PH reaction of ArH^+ (Roueff et al. 2014; Priestley et al. 2017). Priestley et al. (2017) did not consider the PH reaction of HeH^+ because their input SED has negligible flux beyond the Lyman limit relevant for the cross section given by Roberge & Dalgarno (1982). Güsten et al. (2019) also ignored it as the reaction progresses very slowly. We consider the PH reaction of HeH^+, according to Neufeld et al. (2020), which is automatically controlled in Cloudy default network.

Table 4
Gas-phase Elemental Abundances of Species with Respect to Total Hydrogen Nuclei in All Forms for the Modeling of Diffuse ISM in Cloudy

Element	Abundance	Element	Abundance
H	1.00	^{36}Ar	2.82×10^{-6}
He	0.098	^{38}Ar	5.13×10^{-7}
C	2.51×10^{-4}	^{40}Ar	8.20×10^{-10}
N	7.94×10^{-5}	^{20}Ne	1.23×10^{-4}
O	3.19×10^{-4}	^{22}Ne	9.04×10^{-6}
Cl	1.00×10^{-7}	S	3.24×10^{-5}
Mg	1.26×10^{-5}	Fe	6.31×10^{-7}
Si	3.16×10^{-6}		

Note. For the initial isotopic ratio of argon and neon, we have used $^{36}Ar/^{38}Ar/^{40}Ar = 84.5946/15.3808/0.0246$ and $^{20}Ne/^{21}Ne/^{22}Ne = 92.9431/0.2228/6.8341$, following Wieler (2002).

4. Results and Discussions on Chemical Modeling

Reaction pathways for the formation and destruction of noble-gas-related species are already discussed in Section 3. Based on this network, we studied the chemical evolution of the hydride and hydroxyl cations of Ar, Ne, and He. Schilke et al. (2014) assigned absorption lines of ArH^+ to the previously unidentified absorption lines. Though we mainly focus here on the Crab environment, it will be very useful to first check our model with the model described in Schilke et al. (2014) and Priestley et al. (2017) for the diffuse ISM. It will be also useful to look at the predicted abundances of other hydride and hydroxyl cations in diffuse cloud conditions as well.

4.1. Diffuse Interstellar Medium

Here, we assumed a cloud with the initial number density of total hydrogen nuclei (n_H) of 50 cm^{-3} and a primary cosmic-ray ionization rate for atomic hydrogen of $\zeta_H = 2 \times 10^{-16}$ s^{-1} (Schilke et al. 2014). We considered the default ISM elemental abundances of Cloudy, which are shown in Table 4. The unextinguished local interstellar radiation field (ISRF) is generated with the keyword *Table 1SM* in Cloudy. We used the mean ISRF (Draine 1978) of 1 Draine unit, and the resultant shape of the incident SED is further modified by including the extinction due to photoelectric absorption by a cold neutral slab with a column density of $N(H) = 10^{20}$ cm^{-2} (Figure 2). Using the default ISM grain and the H_2 grain formation rate of 3×10^{-17} cm^3 s^{-1} (Jura 1975) and by considering the default PAH treatment in Cloudy, we obtained an extinction-to-gas ratio of $A_V/N(H) = 5.412 \times 10^{-22}$ mag cm^2 for this region.

Figure 4 shows the abundances of some of the important species considered in our network as a function of the visual extinction, A_V. Throughout the region, the cloud remains in atomic form, and the H_2 fractional abundance varies between 2×10^{-5} and 10^{-1}. The electron temperature varies in the range 25–50 K, and the electron fractional abundance remains roughly invariant at $\sim 10^{-3}$. The peak abundance of ArH^+ is around 1.3×10^{-9}, decreasing with increasing A_V deep inside the cloud. ArH^+ is a unique tracer of the atomic gas, having a H_2 fractional abundance of 10^{-4}–10^{-3} (Schilke et al. 2014). We find a very similar result here. Deep inside the filament, where the H_2 density is sufficiently increased, a strong anticorrelation is present between ArH^+ and H_2. The abundance profile of ArH^+ shows a strong anticorrelation with OH^+ and H_2O^+. It implies that while ArH+ traces the region

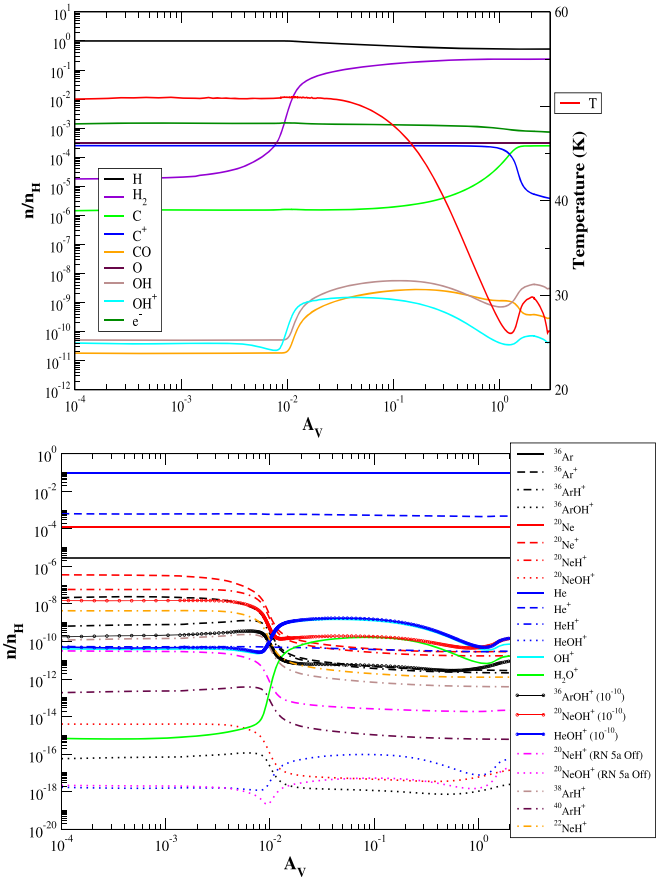

Figure 4. Variation of abundances for simple species with a diffuse ISM model shown in the upper panel. On the right side of the upper panel, the electron temperature variation is shown. In the lower panel, the variation of isotopic abundances for noble gas species is shown. The abundances of $^{36}ArOH^+$, $^{20}NeOH^+$, and $HeOH^+$, considering the upper limit of their formation rate by radiative association reactions ($\sim 10^{-10}$ cm^3 s^{-1}), are noted [XOH^+ (10^{-10})]. The abundance profiles of $^{20}NeH^+$ and $^{20}NeOH^+$ are also shown when reaction 5a of the Ne chemistry network is off.

with lower H_2/H, OH^+ and H_2O^+ favor the higher H_2/H region. The obtained abundances of Ar^+ and ArH^+ match those measured by Schilke et al. (2014) and present a similar variation to A_V. For similar conditions, Priestley et al. (2017) found a slightly lower abundance of these species. NeH^+ also follows the similar behavior of ArH^+, and a strong anticorrelation with H_2 is observed. We obtain a peak fractional abundance of $NeH^+ \sim 5 \times 10^{-8}$. Table 4 shows that Ne has a higher initial elemental abundance than Ar (Ne/Ar = 43.6). This is also reflected in the obtained peak abundance ratio between NeH^+ and ArH^+ ($\sim$38). However, the much higher initial elemental abundance of He than that of the Ar and Ne is not reflected in the obtained abundance of HeH^+. The obtained HeH^+ fractional abundance is smaller (peak abundance 5×10^{-11}) than that of ArH^+ and NeH^+. This is because ArH^+ and NeH^+ formation by $X^+ + H_2 \rightarrow XH^+ + H$ (reaction numbers 5 of Ar and 5a of the Ne chemistry network) is considered, which is avoided in the case of HeH^+ formation here.

Theis et al. (2015) questioned the formation of NeH^+ by reaction 5a. They also found that the possible product of this reaction would be Ne and H_2^+ ($Ne^+ + H_2 \rightarrow Ne + H_2^+$ i.e., reaction 5(c) of the Ne chemistry network). Here, for the diffuse cloud model, we found that the majority of NeH^+ is

Table 5
Comparison between the Obtained Column Densities of Some Atomic and Molecular Ions with the Observation of a Diffuse Cloud toward W51 (Indriolo et al. 2012)

Species	Column Density (cm^{-2})	
	Model	Observation
H	3.02×10^{21}	$(1.39 \pm 0.3) \times 10^{21}$
H_2	1.26×10^{21}	$(1.06 \pm 0.52) \times 10^{21}$
H_3^+	3.52×10^{13}	$(2.89 \pm 0.37) \times 10^{14}$
OH^+	9.04×10^{11}	$(2.97 \pm 0.13) \times 10^{13}$
H_2O^+	1.43×10^{11}	$(6.09 \pm 0.96) \times 10^{12}$
C^+	5.61×10^{17}	$(4.0 \pm 0.4) \times 10^{17}$

formed by the reaction between Ne^+ and H_2 (reaction 5a) and the abundance of NeH^+ is higher than that of ArH^+. However, NeH^+ is yet to be identified in the diffuse region. This also suggests an overestimation of the NeH^+ abundance in our model. In order to check the effect of reaction 5a, we considered the case where this reaction is switched off (unless otherwise stated, this reaction is on by default in all the cases reported in this paper). In this case, we found that the abundance of NeH^+ significantly dropped and is consistent with its absence in the observed spectra (having a peak fractional abundance of $\sim 3 \times 10^{-11}$). The formation of the majority of NeH^+ in this case happens via reaction 14 ($HeH^+ + Ne \rightarrow NeH^+ + He$) of the Ne chemistry network. However, in this case, we have also seen the anticorrelation between NeH^+ and H_2.

According to the recent work by Theis & Fortenberry (2016), the hydroxyl cations of noble gas are the most stable small noble gas molecules analyzed, besides their respective hydride diatomic cation cousins. So, we included them in our network and plotted them here to show the comparison between them. When reaction 5a of the Ne chemistry network is on, the abundance profile of $ArOH^+$ and $NeOH^+$ follows the ArH^+ and NeH^+ abundance profiles because a majority of them form by $ArH^+ + O$ and $NeH^+ + O$ (reaction 13 of the Ar and Ne chemistry network), respectively. The abundance profile of $HeOH^+$ follows the abundance profile of OH due to the formation of the majority of $HeOH^+$ by He^+ and OH. When reaction 5a of the Ne chemistry network is off, we found a similar abundance profile of $NeOH^+$ with $HeOH^+$. Figure 4 also shows the abundances of $ArOH^+$, $NeOH^+$, and $HeOH^+$ by considering the upper limit of their formation rate by radiative association reactions ($\sim 10^{-10}\,cm^3\,s^{-1}$; see Section 3.3 for the justification). A noticeable production of hydroxyl ions was observed only when the upper limit of the rate coefficients was used. A comparison between the obtained column densities of some atomic and molecular ions with the observation of a diffuse cloud toward W51 is shown in Table 5. We found that our results are very close to the observed results.

Here, we also include the ^{38}Ar, ^{40}Ar, ^{20}Ne, and ^{22}Ne isotopes in our network. $^{21}NeH^+$ is not considered here because in the CDMS/JPL database, corresponding spectral information was absent. For the initial isotopic ratio of argon and neon, we have used $^{36}Ar/^{38}Ar/^{40}Ar = 84.5946/15.3808/0.0246$ and $^{20}Ne/^{22}Ne = 13.6$ (Wieler 2002). We found that the peak fractional abundance of $^{38}ArH^+$, $^{40}ArH^+$, and $^{22}NeH^+$ is 2.2×10^{-10}, 3.8×10^{-13}, and 4.5×10^{9}, respectively. This yields a ratio of the peak abundance of $^{36}ArH^+/^{38}ArH^+/^{40}ArH^+ = 84.5946/14.32/0.0247$ and $^{20}NeH^+/^{22}NeH^+ = 11.11/1.0$ (reaction 5a of the Ne chemistry network is considered here). Because no fractionation reactions were considered in this work, initial elemental abundances were roughly reflected in the abundances of their respective hydride ions.

4.2. The Crab Nebula Filament

Physical conditions suitable for the Crab environment are already presented in Section 2. Figure 5 shows the variation of the abundances of the different ionization states of the primary isotope of the noble gas ions (X = ^{36}Ar, ^{20}Ne, and He) as a function of the visual extinction (A_V) for Model A. For this case, we considered the initial model of the Crab with a total hydrogen nuclei density $n_H = 1900\,cm^{-3}$ and cosmic-ray ionization rate per H_2 $\zeta = \zeta_0 = 1.3 \times 10^{-17}\,s^{-1}$. This ζ value is too low for a supernova remnant; more realistic values will be explored in following sections. Here, we used this value because it is the standard value used in chemical models of molecular clouds and used in the initial model of Priestley et al. (2017). In the three blocks of Figure 5, we show three noble-gas-related (Ar, Ne, and He) species. We find that reaction numbers 1–2 of all reaction sets in Table 3 and reaction numbers 27–28 of Ar, 28–29 of Ne, and 19–20 of He are responsible for producing X^+ from X. X^+ is further converted into X^{++} by direct X-ray ionization. X^{++} can further be produced directly from X by direct X-ray ionization. In all blocks of Figure 5, we obtain a higher abundance of X^+ compared to X^{++}. Here, we use the initial elemental abundance of ^{36}Ar, ^{20}Ne, and He of 1.0×10^{-5}, 4.9×10^{-3}, and 1.85, respectively, with respect to total hydrogen nuclei in all forms (see Table 2). This initial elemental abundance ratio between the noble gases is not maintained after they have formed their respective hydride ions. If they were following their initial abundances, then the abundance of ArH^+ would have been of $\sim 10^5$ times lower than that of the HeH^+ ion. Instead, from Figure 5, we obtain the peak abundance of ArH^+, NeH^+ (when Ne reaction 5a is off), and HeH^+ in a similar range. The reason behind this is due to (i) the lower ionization potential of ^{36}Ar (15.76 eV) compared to ^{20}Ne (21.5645 eV) and He (24.5874 eV), (ii) the high proton affinity of Ar (3.85 eV) compared to Ne (2.08 eV) and He (1.85 eV; Jolly 1984), and (iii) the reaction pathways adopted.

In the early universe, HeH^+ formation was dominated by the reaction between He and H^+. Due to their high ionization potential, helium ions (He^+ and He^{+2}) recombined with electrons to produce neutral helium first. Neutral helium was indeed the first neutral atom of the universe. In such a metal-free situation, He then reacted with H^+ to form the first chemical bond of the universe ($He + H^+ \rightarrow HeH^+ + h\nu$) and thus the first molecule, HeH^+. Recently, Güsten et al. (2019) identified the pure rotational ($J = 1$–0) transition of HeH^+ in the planetary nebula NGC 7027. But the formation of HeH^+ in the planetary environment progresses in a very different manner. Looking at the environment of NGC 7027 and its age, they ignored the HeH^+ formation by $He + H_2^+ \rightarrow HeH^+ + H$ as well as with $He + H^+ \rightarrow HeH^+ + h\nu$ (reaction numbers 3 and 16, respectively, of the He network in Table 3). Neufeld et al. (2020) considered reactions 3 and 16 of the He chemistry in their network. Here, we used their adopted rate in our simulation. Additionally, we also considered $He^+ + H \rightarrow HeH^+ + h\nu$ (reaction number 15) following Güsten et al. (2019). The reaction between Ar and H_3^+ (reaction 4) was considered by Priestley et al. (2017) in their model. We examined XH^+ formation by this reaction quantum-chemically (discussed in Section 3.2).

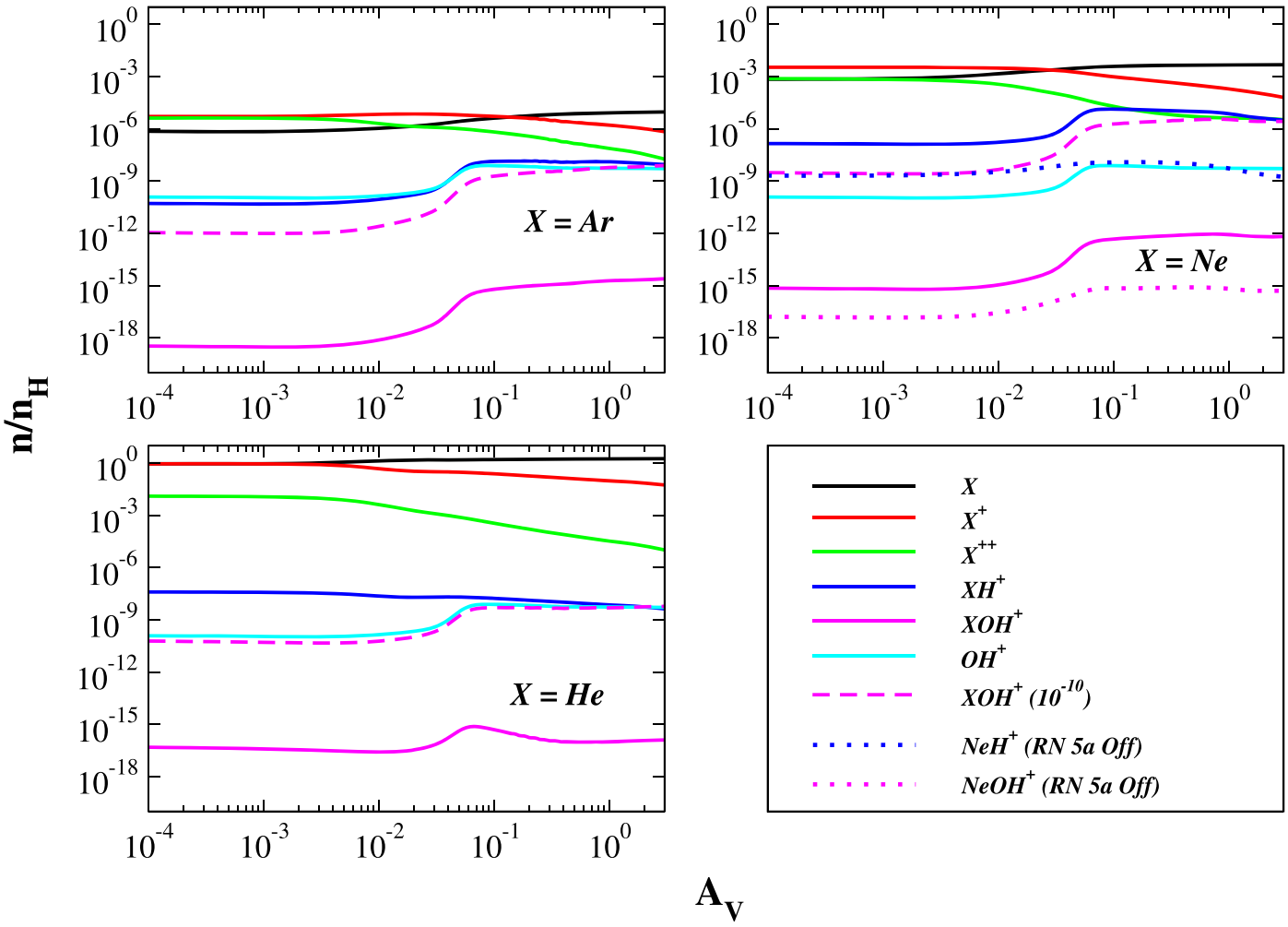

Figure 5. Abundances of various ionized states of noble gas (X = ^{36}Ar, ^{20}Ne, and He) along with their respective hydride and hydroxyl cations as a function of A_V considering Crab Model A with $n_H = 1900$ cm^{-3} and $\zeta_{H_2} = \zeta_0 = 1.3 \times 10^{-17}$ s^{-1}. The dashed pink lines denote the abundance of XOH$^+$ considering the upper limit of forming XOH$^+$ ($\sim 10^{-10}$ cm^3 s^{-1}; see Section 3.3 for the justification). Abundances of NeH$^+$ and NeOH$^+$ are shown in dotted blue and dotted magenta lines respectively when Ne chemistry reaction 5a is switched off.

We found an endothermicity value of ≈6019 K for the formation of ArH$^+$ by reaction 4, and for the formation of HeH$^+$ and NeH$^+$, the obtained endothermicity value is ∼5 times higher than that of the ArH$^+$. It shows that the formation of HeH$^+$ and NeH$^+$ by reaction 4 is only possible at high temperature (>1000 K). The consideration of very different chemical pathways for the formation of ArH$^+$ compared to HeH$^+$ and NeH$^+$ thus played a significant role for the mismatch between the initial elemental ratio considered and the ratio obtained after the formation of their hydride ions.

The lower limit of the detected OH$^+$ transition in the Crab can be used to set the lower observational limit for the noble gas ions modeled here. To show the comparison between the OH$^+$ abundance and other noble-gas-related species, we have shown the abundance of OH$^+$ in all panels of Figure 5. We obtained a lower peak abundance of OH$^+$ than Priestley et al. (2017). This is indeed required because Barlow et al. (2013) observed the ArH$^+$ transition to be significantly stronger than that of the OH$^+$. Figure 5 shows that ArH$^+$ is initially less abundant than OH+, and finally deep inside the filament it shows the opposite trend.

By considering the same physical condition considered in the case of Figure 5, the abundance variation for some of the important species is shown in Figure 6. The left panel shows the abundance variation of H, H_2, C, C$^+$, CO, OH, and OH$^+$, and the right panel shows the simple ions of H (H$^+$, H_2^+, and H_3^+), electrons, and the variation of the electron temperature. The left panel shows that most of the hydrogen is in atomic form and thus the cloud remains entirely atomic. In the outer part ($A_V < 1$ mag) of the cloud, carbon remains in ionized form (C$^+$), but it is converted into the neutral form inside ($A_V >$ 1 mag) the cloud. Because the cloud is mostly in diffuse atomic form, the CO fractional abundance is $\sim 10^{-10}$. Figure 6 shows that the abundance of H_2 is increasing deep inside the cloud, and Figure 5 shows that the abundance of ArH$^+$ is also increasing deep inside the cloud. Thus, the anticorrelation that has been seen between the abundance profile of ArH$^+$ and H_2 in Figure 4 is not reflected here. This might be due to the consideration of completely different physical-chemical conditions between these two cases. The right panel shows that H$^+$ is very abundant, and the electron abundance varies within a few times 10^{-1} (i.e., electron number density ∼few times 10^2 cm^{-3} for $n_H = 1900$ cm^{-3}), which matches with that of the predicted electron number density in the knot of the Crab (Barlow et al. 2013). In this effort, it is thus essential to find out the physical

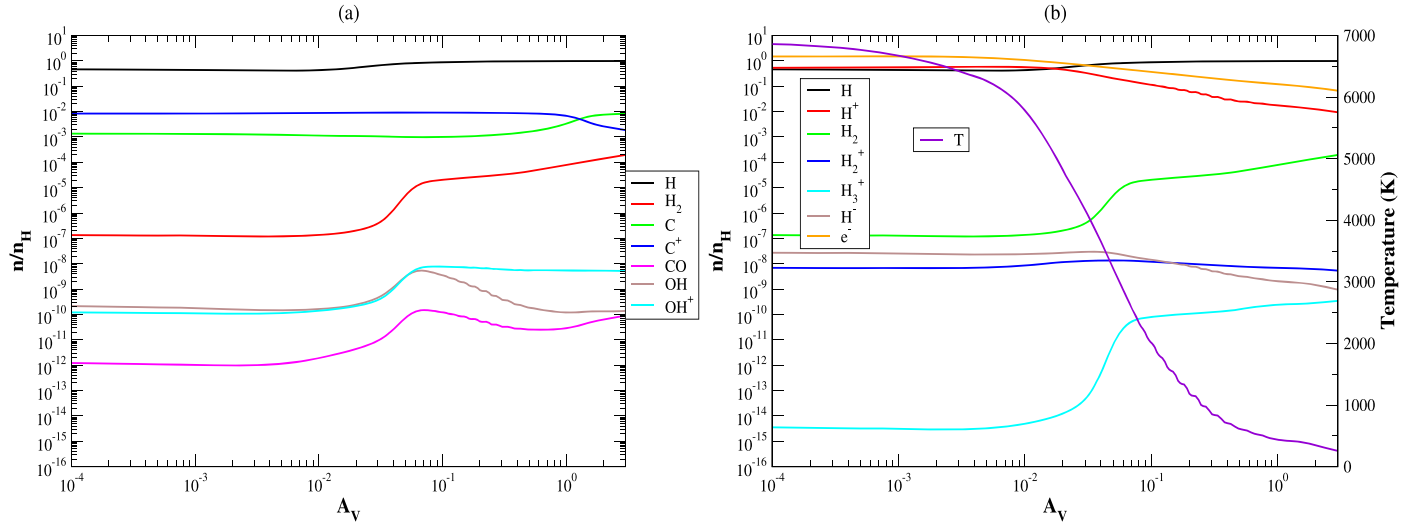

Figure 6. Fractional abundance variation of the simple species with A_V by considering $n_{\rm H} = 1900\ {\rm cm}^{-3}$ and $\zeta_{\rm H_2} = \zeta_0 = 1.3 \times 10^{-17}\ {\rm s}^{-1}$ (Model A). On the right side of the right panel, the electron temperature variation is shown.

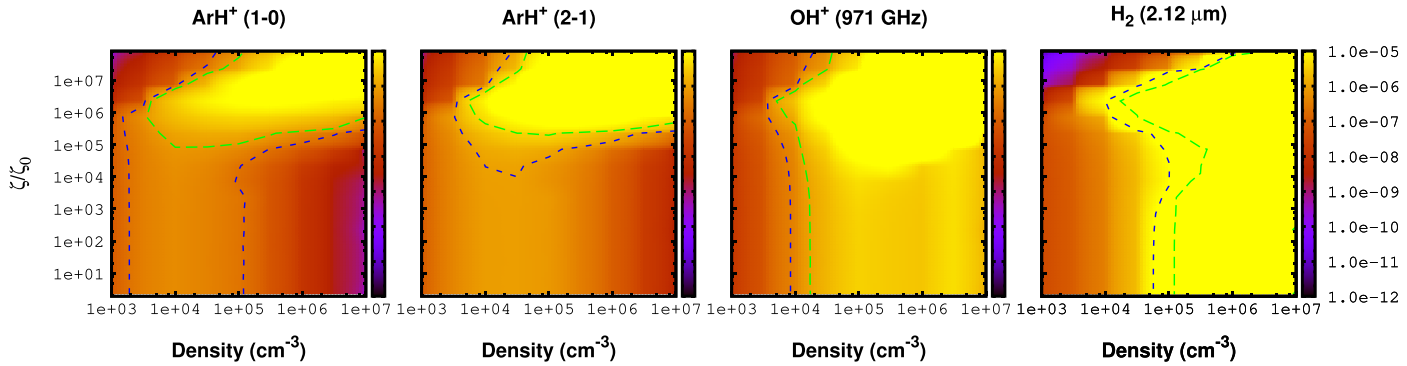

Figure 7. Parameter space for the intrinsic line surface brightness (SB) of the 1−0 and 2−1 transitions of ArH^+, the 971 GHz/308 μm transition of OH^+, and the 2.12 μm transition of H_2 considering Model A. The right panel is marked with the color-coded values of the intrinsic line SB (in units of erg cm^{-2} s^{-1} sr^{-1}). The contours are highlighted in the range of observational limits noted in Table 6 (column 2).

conditions that can possibly explain most of the observational results of Barlow et al. (2013).

4.2.1. Comparison with Observations: Model A

To find out a suitable favorable zone to explain the observed features, we varied the physical parameters ($n_{\rm H}$ and ζ). Our parameter space consists of a density ($n_{\rm H}$) variation of about 10^3–$10^7\ {\rm cm}^{-3}$ and ζ/ζ_0 ($\zeta_0 = 1.3 \times 10^{-17}\ {\rm s}^{-1}$) variation of about 1–$10^8$. Figure 7 shows the absolute surface brightness variation of various transitions with a wide range of parameter space for Model A. In Table 6, we have summarized the observed surface brightness of the two transitions of ArH^+ ($2 \rightarrow 1$ and $1 \rightarrow 0$), the 308 μm (971 GHz, $J = 2 \rightarrow 1$, $F = 5/2 \rightarrow 3/2$) transition of OH^+, and the 2.12 μm transition of H_2 (Barlow et al. 2013; Loh et al. 2011). We obtain a reasonable match of the absolute surface brightness of these transitions with the observation when high values of $\zeta/\zeta_0 \sim 10^6$–10^8 and $n_{\rm H} \sim 10^4$–$10^{5.3}\ {\rm cm}^{-3}$ were considered. In Figure C1 in Appendix C, we show the variation of the absolute surface brightness of these transitions with respect to the variation of a wide range of parameter space (varying ζ/ζ_0 and the core density $n_{\rm H(core)}$) by considering Model B. Moreover, in Table 6, we have listed the results obtained from Model B in explaining the observed absolute surface brightness of these transitions.

Figure 8 shows the surface brightness ratio of several transitions for a wide range of parameter space for Model A. Observational results for this surface brightness ratio are summarized in Table 7. The observed ratio of ∼1–17 (obtained by taking the minimum and maximum values from the observed two transitions of ArH^+) between the two transitions of ArH^+ and the ratio between these two ArH^+ transitions with respect to the OH^+ 971 GHz transition were best reproduced when we considered $\zeta/\zeta_0 \sim 10^7$ with $n_{\rm H} = 10^{4-6}\ {\rm cm}^{-3}$. Because the transitions of CO were not detected, it is expected that the surface brightness ratio of the various transitions of CO with respect to the OH^+ 971 GHz transition would be <1. We also have obtained a lower surface brightness ratio between all the transitions of CO and the 971 GHz transition of OH^+. One of the major drawbacks of our Model A is that we are unable to reproduce the lack of [C I] emissions found by Barlow et al. (2013). This mismatch is due to the high abundance of neutral carbon [C I] in comparison to OH^+ in our Model A. However, our model can successfully explain the lack of CO emission, the 158 μm transition of C^+ [C II], and the relative line strengths between [O I] and [C II]. Similarly, the results obtained with Model B are shown in Figure C2 of Appendix C, and the most suitable zone is highlighted in Table 7.

Table 6
Summary of the Previously Observed Surface Brightness (SB) Values in erg cm^{-2} s^{-1} sr^{-1}

Molecular Transitions	Observational SB Limits[a]	Matching Zone with $\frac{\zeta}{\zeta_0}$ and n_H (cm^{-3})	
		Model A	Model B ($n_H = n_{H(core)}$)[b]
ArH $^+(1-0)$ (617 GHz/485 μm)	(2.2–9.9) $\times$ 10^{-7}	$\frac{\zeta}{\zeta_0} \sim 10^{0-5}$ for $n_H \sim 10^{3-5}$ $\frac{\zeta}{\zeta_0} \sim 10^{6-7}$ for $n_H \sim 3.16 \times 10^4$ $\frac{\zeta}{\zeta_0} \sim 10^7$ for $n_H \sim 10^5$ $\frac{\zeta}{\zeta_0} \sim 10^5$ for $n_H \sim 10^{6-7}$	$\frac{\zeta}{\zeta_0} \sim 10^{0-6}$ for $n_H \sim (3.16 \times 10^3) - 10^5$ $\frac{\zeta}{\zeta_0} \sim 10^{0-7}$ for $n_H \sim (3.16 \times 10^5) - 10^6$
ArH $^+(2-1)$ (1234 GHz/242 μm)	(1–3.8) $\times$ 10^{-6}	$\frac{\zeta}{\zeta_0} \sim 10^{4-7}$ for $n_H \sim 10^{4-5}$ $\frac{\zeta}{\zeta_0} \sim 10^{5-6}$ for $n_H \sim 10^{6-7}$	$\frac{\zeta}{\zeta_0} \sim 10^{0-6}$ for $n_H \sim (3.16 \times 10^3) - 10^5$ $\frac{\zeta}{\zeta_0} \sim 10^{0-7}$ for $n_H \sim (3.16 \times 10^5) - 10^6$
OH^+ (971 GHz/308 μm)	(3.4–10.3) $\times$ 10^{-7}	$\frac{\zeta}{\zeta_0} \sim 10^{0-4}$ for $n_H \sim 10^{4-7}$ $\frac{\zeta}{\zeta_0} \sim 10^{5-7}$ for $n_H \sim 10^4$ $\frac{\zeta}{\zeta_0} \sim 10^7$ for $n_H \sim 10^5$	$\frac{\zeta}{\zeta_0} \sim 10^{0-6}$ for $n_H \sim 3.16 \times 10^{3-5}$ $\frac{\zeta}{\zeta_0} \sim 10^{0-7}$ for $n_H \sim 10^6$
H_2 (2.12 μm)	(1–4.8) $\times$ 10^{-5}	$\frac{\zeta}{\zeta_0} \sim 10^6$ for $n_H \sim 10^4$ $\frac{\zeta}{\zeta_0} \sim 10^{0-5}$ for $n_H \sim 10^5$	$\frac{\zeta}{\zeta_0} \sim 3.54 \times 10^6$ for $n_H \sim (3.16 \times 10^3) - 10^6$

Notes. The most suitable values of n_H and ζ/ζ_0 to explain the observed values are also pointed out.
[a] Priestley et al. (2017) and references therein.
[b] $n_H = n_{H(core)}$ indicates the core density for Model B (see Section 2 for details).

With Model B, we are able to successfully explain most of the observed features. Even the lack of [C I] emission is also well explained by this model.

From Figures 7–8 and Tables 6–7, it is very difficult to arrive at the best suitable parameter for n_H and ζ/ζ_0 that can reproduce all the observational results simultaneously. However, from Model A, we have two favorable matching zones at $n_H \sim 10^{4-5}$ cm^{-3} and $\zeta/\zeta_0 \sim 10^{6-7}$, and for Model B, we found that the values used by Richardson et al. (2013) for their ionizing particle model $n_{H(core)} \sim 10^{5-6}$ cm^{-3} and $\zeta/\zeta_0 \sim 10^{6-7}$ are favorable. So, in general, in terms of the absolute intrinsic surface brightness and surface brightness ratio, we find our favorable parameter space with $n_H \sim 10^{4-6}$ and higher $\zeta/\zeta_0 = 10^{6-7}$.

In between the favorable zone of Model A, we further consider $n_H = 2.00 \times 10^4$ cm^{-3} and $\zeta = 9.07 \times 10^6 \zeta_0$ as Model A1 to suitably match the absolute surface brightness of the two transitions of $^{36}ArH^+$ (242 and 485 μm) and the 308 μm transition of OH^+ simultaneously, and $n_H = 3.16 \times 10^4$ cm^{-3} and $\zeta = 4.55 \times 10^6 \zeta_0$ as Model A2 to suitably match the absolute surface brightness of H_2 of 2.12 μm separately. Unless otherwise stated, Model A1 is always used in all the cases reported throughout this paper. Figure 9 shows the abundance variation of the simple species, along with the density of electrons and the electron temperature of the Crab. It is clear from the figure that the temperature of the Crab region is 4000 K and the electron abundance is >0.1, which is in line with the observation of Barlow et al. (2013). A suitably high fractional abundance of H_2 ($\sim 10^{-6}$) is observed, which is capable of explaining the H_2 surface brightness in the knots of the Crab. Additionally, we show the abundances of H_2^+ and H_3^+. In Figure 10(a), the abundances of Ar-related species along with their isotopologs are shown, whereas in Figure 10(b), the abundances of the He- and Ne-related (and its isotopologs) species are shown. We did not consider any fractionation reaction between the isotopologs of Ar and Ne. Due to this reason, the elemental abundance ratio is reflected in the molecular abundances of the various isotopologs. OH^+ had been identified in the emitting knots of the Crab. So, the observability of the species may be compared to the OH^+ abundance. Both panels of Figure 10 show the OH^+ abundance to understand the fate of other chemical species for future identification in the Crab emitting knots. Figures 10(a) and (b) clearly depict how the abundances of $^{36}ArH^+$, $^{20}NeH^+$ (even in the absence of reaction 5a, we obtained a comparable abundance of $^{20}NeH^+$ with OH^+; see Figure 10(b)), and HeH^+ are higher than those of OH^+, and thus $^{20}NeH^+$ and HeH^+ could have been observed in the Crab emitting knots. However, even with the upper limit of the rate coefficient, we always obtained a lower abundance of hydroxyl ions ($^{36}ArOH^+$, $^{20}NeOH^+$, and $HeOH^+$) compared to OH^+.

Similarly, the abundance profiles obtained with Model B are shown in Appendix C (see Figures C3 and C4). It is interesting to note that for this case, we have obtained a much higher electron temperature (>10000 K) that can yield a better estimation for the various atomic transitions listed in Table 8.

The emissivity of some of the prominent transitions that fall in between the frequency regime of Herschel's SPIRE and Photodetecting Array Camera and Spectrometer (PACS) and SOFIA are shown in Figure 11 for Model A1. Barlow et al. (2013) found that the 2–1 and 1–0 transitions of $^{36}ArH^+$ were significantly stronger than those of OH^+. From Figure 11, we find that in most of the region, the 971 GHz (308 μm) transition of OH^+ (the strongest transition of OH^+ in such a condition) is stronger than that of the 1–0 transition (617 GHz/485 μm) and weaker than the 2–1 transition (1234 GHz/242 μm) of ArH^+. This is partly consistent with the observation of Barlow et al. (2013). Barlow et al. (2013) also found the $J = 2-1$ transition (1234 GHz/242 μm) stronger than the $J = 1-0$ (617 GHz/485 μm). We find the same trend in Figure 11. Barlow et al. (2013) detected only the 971 GHz (308 μm) transition, which was

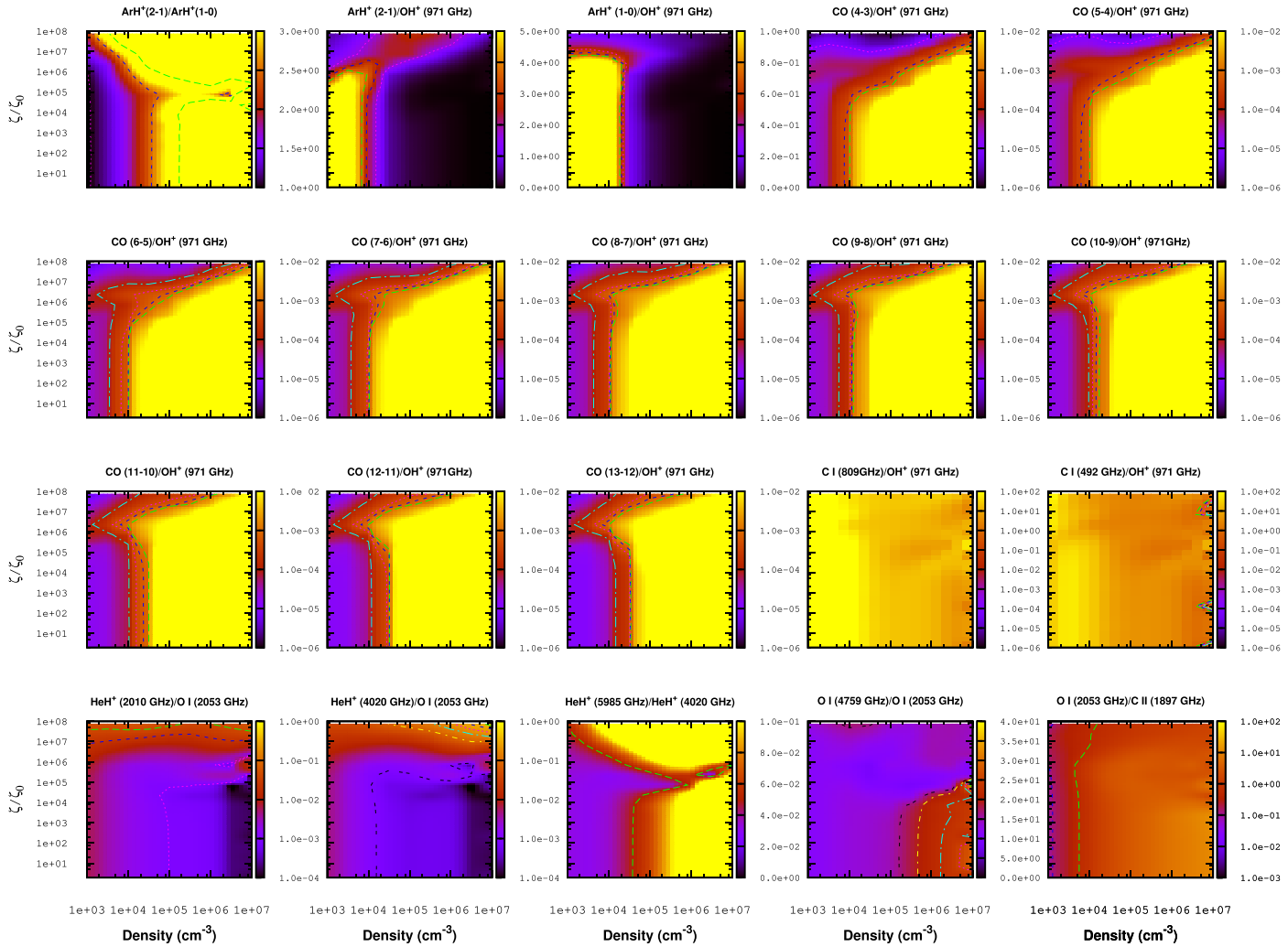

Figure 8. Intrinsic line surface brightness (SB) ratio of various molecular and atomic transition fluxes considering Model A. The right side of each panel is marked with color-coded values of the intrinsic line SB ratio. The contours are highlighted around the previously observed or estimated SB ratios noted in Table 7 (column 2).

comparable to the $J = 1-0$ (617 GHz/485 μm) transition of $^{36}ArH^+$. From our model, we can see that the 1−0 transition of $^{36}ArH^+$ is comparable to the 971 GHz transition of OH^+ deep inside the filament. The emissivity of the XOH^+ (X = Ar, Ne, and He) transitions, which fall in between the 29–1409 GHz region, is shown in Figure 12. These transitions could be very useful for the future astronomical detection of these species around similar environments, where strong OH^+ emission had already been identified.

In Table 9, we have listed the strongest transitions that fall in the observed range of Herschel's SPIRE and PACS spectrometer and also within the range of SOFIA, ALMA, Very Large Array (VLA), Institute for Radio Astronomy in the Millimeter Range (IRAM) 30 m, and Northern Extended Millimeter Array (NOEMA). The optical depth of all these transitions is also noted. For this calculation, we used the RADEX program by considering only electrons as colliding partners. We consider $n_e = 10^3\,cm^{-3}$ and temperature 2700 K. The radiation field shown in Figure 1(c) is considered as the background radiation field. The total column density of the species is also noted from the calculation with $n_H = 2.00 \times 10^4\,cm^{-3}$ and $\zeta/\zeta_0 = 9.07 \times 10^6$ (Model A1). Similarly, the emissivity obtained with Model B is shown in Figures C5 and C6.

Barlow et al. (2013) obtained a surface brightness of ∼(2.2–9.9) × 10^{-7} erg cm^{-2} s^{-1} sr^{-1} for the 1 → 0 transition of $^{36}ArH^+$ (617 GHz/485 μm) whereas our best-fitted Model A (i.e., Model A1) finds ∼2.84 × 10^{-7} erg cm^{-2} s^{-1} sr^{-1}. For the 2 → 1 transition of $^{36}ArH^+$, Barlow et al. (2013) obtained a surface brightness of ∼(1.0–3.8) × 10^{-6} erg cm^{-2} s^{-1} sr^{-1}, whereas our best-fitted model finds ∼1.29 × 10^{-6} erg cm^{-2} s^{-1} sr^{-1}. Priestley et al. (2017) checked the detectability of these transitions based on the observed surface brightness of the 971 GHz (308 μm) transition of OH^+. Barlow et al. (2013) obtained the surface brightness of the 971 GHz transition of ∼(3.4–10.3) × 10^{-7} erg cm^{-2} s^{-1} sr^{-1} whereas our best-fitted model finds it to be ∼6.17 × 10^{-7} erg cm^{-2} s^{-1} sr^{-1}. Thus, our best-fitted model (Model A1) always predicts a comparable or stronger surface brightness of $^{36}ArH^+$ transitions (242 and 485 μm) in comparison to the 308 μm transition of OH^+, which is consistent with the results. Now, to examine the detectability of the other transitions of $^{36}ArH^+$ and for other hydride ions along with their isotopic forms considered in this study, we check three criteria for each transition: (i) whether the surface brightness of that transition is comparable to or stronger than the observed surface brightness of the 308 μm transition of OH^+, (ii) the presence of atmospheric transmission (calculated by the ATRAN program of Lord 1992) at the height of ∼41,000 ft (i.e., at the height of SOFIA), and (iii)

Table 7
Summary of the Previously Observed or Estimated Line Surface Brightness (SB) Ratios

Transition Ratios	Observed or Estimated SB ratios	Matching Zone with $\frac{\zeta}{\zeta_0}$ and $n_{\rm H}$ ($\rm cm^{-3}$)	
		Model A	Model B ($n_{\rm H} = n_{\rm H(core)}$)[a]
$\frac{\rm ArH^+\ (2-1)}{\rm ArH^+\ (1-0)}$	2[b] (1–17)[c]	$\frac{\zeta}{\zeta_0} \sim 10^{6-8}$ for $n_{\rm H} \sim 10^3$ $\frac{\zeta}{\zeta_0} \sim 10^{0-7}$ for $n_{\rm H} \sim 10^4$ $\frac{\zeta}{\zeta_0} \sim 10^{0-5}$ for $n_{\rm H} \sim 10^5$ $\frac{\zeta}{\zeta_0} \sim 10^{4-5}$ for $n_{\rm H} \sim 10^{6-7}$	$\frac{\zeta}{\zeta_0} \sim 10^{0-7}$ for $n_{\rm H} \sim (3.16 \times 10^3) - 10^5$ $\frac{\zeta}{\zeta_0} \sim 10^{0-6}$ for $n_{\rm H} \sim (3.16 \times 10^5) - 10^6$
$\frac{\rm ArH^+\ (2-1)}{\rm OH^+(971\ GHz/308\ \mu m)}$	1.66–3.9[b] (1–11)[c]	$\frac{\zeta}{\zeta_0} \sim 10^5$ for $n_{\rm H} \sim 10^3$ $\frac{\zeta}{\zeta_0} \sim 10^{0-7}$ for $n_{\rm H} \sim 10^4$ $\frac{\zeta}{\zeta_0} \sim 10^{6-8}$ for $n_{\rm H} \sim 10^{5-6}$	$\frac{\zeta}{\zeta_0} \sim 10^{0-4}$ for $n_{\rm H} \sim (3.16 \times 10^3) - 10^4$ $\frac{\zeta}{\zeta_0} \sim 10^{0-6}$ for $n_{\rm H} \sim 10^{5-6}$
$\frac{\rm ArH^+\ (1-0)}{\rm OH^+(971\ GHz/308\ \mu m)}$	0.56–0.8[b] (0.21–2.91)[c]	$\frac{\zeta}{\zeta_0} \sim 10^6$ for $n_{\rm H} \sim 10^{3-4}$	$\frac{\zeta}{\zeta_0} \sim 10^7$ for $n_{\rm H} \sim (3.16 \times 10^3) - 10^6$ $\frac{\zeta}{\zeta_0} \sim 10^{4-5}$ for $n_{\rm H} \sim 3.16 \times 10^5$ $\frac{\zeta}{\zeta_0} \sim 10^{0-7}$ for $n_{\rm H} \sim 10^6$
$\frac{\rm CO\ (4-3,\ 5-4,\ldots,13-12)}{\rm OH^+(971\ GHz/308\ \mu m)}$	$\ll 1$[d]	$\frac{\zeta}{\zeta_0} \sim 10^{0-6}$ for $n_H \sim 10^{3-4}$ $\frac{\zeta}{\zeta_0} \sim 10^{5-8}$ for $n_H \sim 10^{5-7}$	$\frac{\zeta}{\zeta_0} \sim 10^{0-7}$ for $n_{\rm H} \sim (3.16 \times 10^3) - 10^5$ $\frac{\zeta}{\zeta_0} \sim 10^{5-7}$ for $n_{\rm H} \sim 10^6$
$\frac{\rm C\ I\ (809\ GHz/370\ \mu m)}{\rm OH^+(971\ GHz/308\ \mu m)}$	<1[d]	$\frac{\zeta}{\zeta_0} \sim 3.13 \times 10^2$ for $n_{\rm H} \sim 10^7$	$\frac{\zeta}{\zeta_0} \sim 10^{0-6}$ for $n_{\rm H} \sim (3.16 \times 10^3) - 10^6$
$\frac{\rm C\ I\ (492\ GHz/609\ \mu m)}{\rm OH^+(971\ GHz)/308\ \mu m}$	<1[d]	$\frac{\zeta}{\zeta_0} \sim 10^{3,5,7}$ for $n_{\rm H} \sim 10^7$	$\frac{\zeta}{\zeta_0} \sim 10^{0-6}$ for $n_{\rm H} \sim (3.16 \times 10^3) - 10^6$
$\frac{\rm HeH^+\ (1–0,\ 2010\ GHz/149\ \mu m)}{\rm O\ I\ (2053\ GHz/146\ \mu m)}$	<1[e]	$\zeta/\zeta_0 \sim 10^{0-8}$ for $n_{\rm H} \sim 10^{3-7}$	$\frac{\zeta}{\zeta_0} \sim 10^{0-8}$ for $n_{\rm H} \sim (3.16 \times 10^3) - 10^6$
$\frac{\rm HeH^+\ (2-1,\ 4020\ GHz/74\ \mu m)}{\rm O\ I\ (2053\ GHz/146\ \mu m)}$	<1[e]	$\frac{\zeta}{\zeta_0} \sim 10^{0-8}$ for $n_{\rm H} \sim 10^{3-7}$	$\frac{\zeta}{\zeta_0} \sim 10^{0-8}$ for $n_{\rm H} \sim (3.16 \times 10^3) - 10^6$
$\frac{\rm HeH^+(3-2,\ 5985\ GHz/50\ \mu m)}{\rm HeH^+(2-1,\ 4020\ GHz/74\ \mu m)}$	$\sim$0.05[e]	$\frac{\zeta}{\zeta_0} \sim 10^{4-6}$ for $n_{\rm H} \sim 10^{6-7}$	$\frac{\zeta}{\zeta_0} \sim 10^5$ for $n_{\rm H} \sim 3.16 \times 10^{3-4}$ $\frac{\zeta}{\zeta_0} \sim 10^{5-6}$ for $n_{\rm H} \sim 10^{5-6}$
$\frac{\rm O\ I\ (4758\ GHz/63\ \mu m)}{\rm O\ I\ (2053\ GHz/146\ \mu m)}$	16.4–38.7[f]	$\frac{\zeta}{\zeta_0} \sim 10^8$ for $n_{\rm H} \sim 10^{4-5}$ $\frac{\zeta}{\zeta_0} \sim 10^{0-4}$ for $n_{\rm H} \sim 10^{6-7}$	$\frac{\zeta}{\zeta_0} \sim 10^{0-8}$ for $n_{\rm H} \sim (3.16 \times 10^3) - 10^6$
$\frac{\rm O\ I\ (2053\ GHz/146\ \mu m)}{\rm C\ II\ (1897\ GHz/158\ \mu m)}$	0.125–0.323[f]	$\frac{\zeta}{\zeta_0} \sim 10^{5-8}$ for $n_{\rm H} \sim 10^{3-4}$	$\frac{\zeta}{\zeta_0} \sim 10^{0-4}$ for $n_{\rm H} \sim (3.16 \times 10^3) - 10^6$

Notes. The most suitable values of $n_{\rm H}$ and ζ/ζ_0 to explain the listed SB values are also pointed out.
[a] $n_{\rm H} = n_{\rm H(core)}$ indicates the core density for Model B (see Section 2 for details).
[b] Priestley et al. (2017) and references therein.
[c] Taking the ratio with the observed maximum and minimum surface brightness between the two transitions noted in Table 6.
[d] Priestley et al. (2017); weak enough to be consistent with the observation.
[e] Prediction from the model of Priestley et al. (2017).
[f] Gomez et al. (2012).

the optical depth of that transition. With the ground-based telescope, transitions falling in between 30 and 650 μm are heavily affected by the atmospheric transmission. For example, at the ALMA site, the amount of precipitable water vapor is typically 1.0 mm, falling below 0.25 mm up to 5% of the time. All transitions of $^{36}\rm ArH^+$ reported in this paper are falling in this range (69–486 μm), and thus, it is difficult to observe these transitions with any ground-based telescope. However, with a space-based telescope, it is possible to detect some more transitions of this species.

To clearly show the detectability of these transitions, in Figure 13(a), we show the surface brightness of these transitions

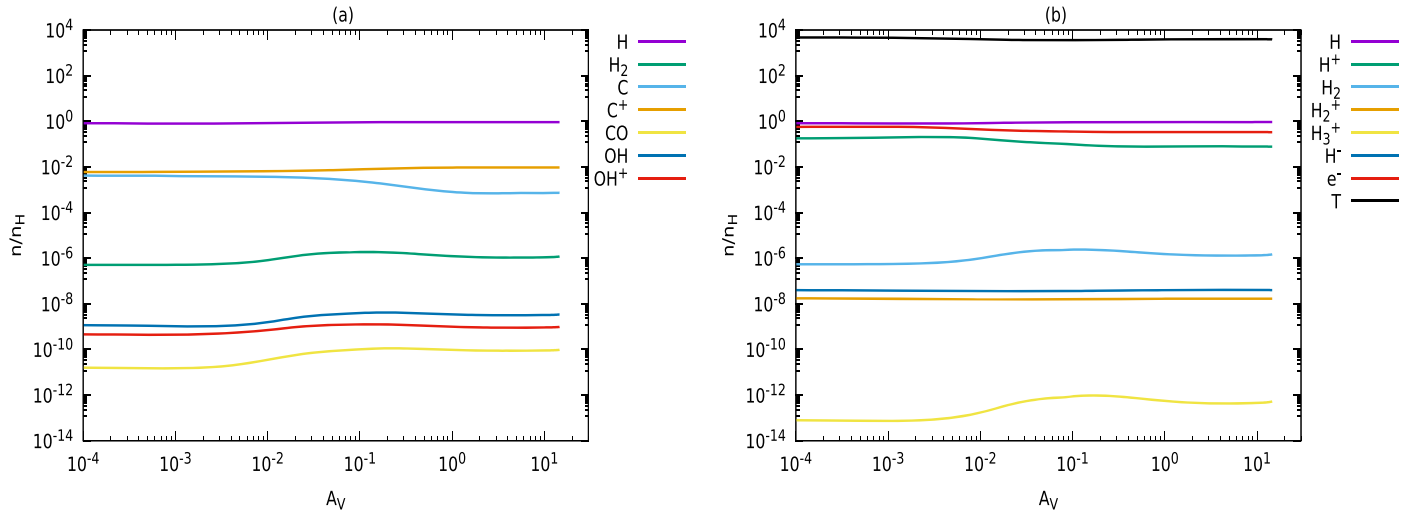

Figure 9. Abundance variation of simple species with A_V considering $n_{\rm H} = 2.00 \times 10^4$ cm^{-3} and $\zeta/\zeta_0 = 9.07 \times 10^6$ (Model A1).

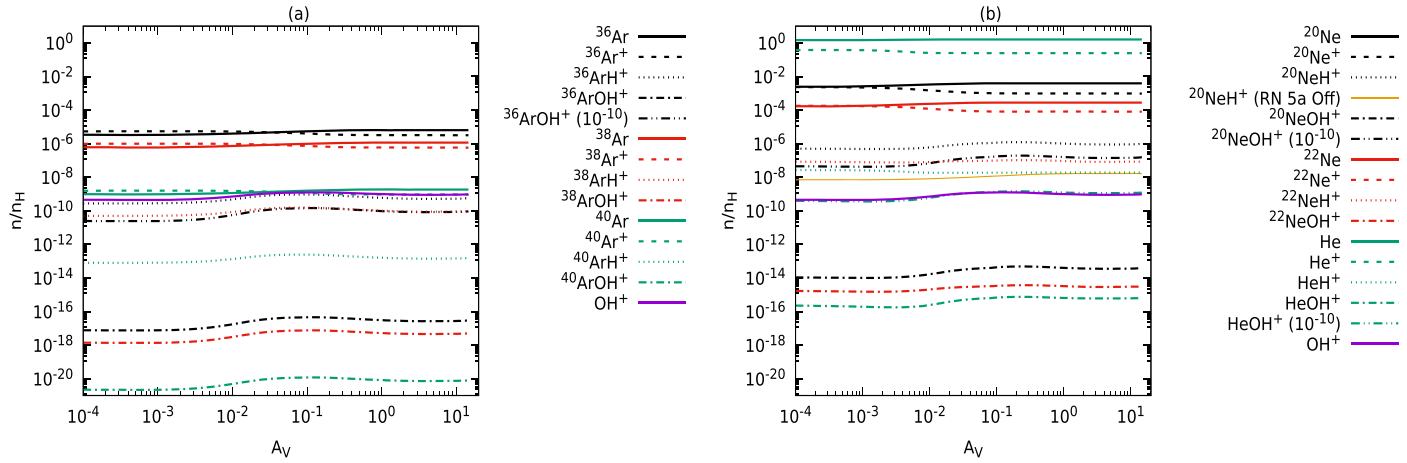

Figure 10. Abundance variation of all the hydride and hydroxyl cations considered in this work by considering $n_{\rm H} = 2.00 \times 10^4$ cm^{-3} and $\zeta/\zeta_0 = 9.07 \times 10^6$ (Model A1). In the left panel (a), Ar-related species are shown, and in the right panel (b) the cases of Ne and He are shown. The abundance variation of OH^+ is shown in both panels for comparison. The abundances of $^{36}ArOH^+$, $^{20}NeOH^+$, and $HeOH^+$ by considering the upper limit of their formation rate ($\sim 10^{-10}$ cm^3 s^{-1}) are noted [XOH^+ (10^{-10})]. The abundance profile of $^{20}NeH^+$ is also shown when reaction 5a of the Ne chemistry network is off.

obtained from our best-fitted Model A1 along with the observed 308 μm transition of OH^+. Table 9 clearly shows that all these transitions have optical depth <1. Figure 13(a) shows that the first five transitions are stronger relative to the observed 917 GHz (308 μm) transition of OH^+. Among them, the 617 GHz (485 μm) and 1234 GHz (242 μm) transitions were already observed by Herschel, which is no longer operational. Among the other three transitions of $^{36}ArH^+$, we can see that 2465 GHz (121 μm) and 3078 GHz (97 μm) are heavily affected by the atmospheric transmission and thus difficult to observe. But the $3 \rightarrow 2$ transition at 1850 GHz (162 μm) is far from atmospheric absorption features and falls in the range of the LFA receiver of the modular heterodyne instrument GREAT of SOFIA. However, with the SOFIA instrument time estimator, we found a long integration time required for this transition. We expect that with Herschel, the chance of detection would have been higher.

A similar analysis was carried out for $^{20}NeH^+$ and HeH^+. When we considered $Ne^+ + H_2 \rightarrow NeH^+ + H$ (reaction 5a) for the formation of NeH^+, we obtained a higher abundance of $^{20}NeH^+$ and called it an upper limit. In the absence of this reaction, we obtained a lower limit of the NeH^+ formation. With the upper limit of its formation, Table 9 shows that the 1039 GHz (288 μm), 2076 GHz (144 μm), and 3110 GHz (96 μm) transitions have an optical depth >1. For the other four transitions, it is <1. Figure 13(b) shows that the other four transitions at 4137 GHz (72 μm), 5157 GHz (58 μm), 6167 (48 μm), and 7166 GHz (42 μm) are showing a comparatively stronger surface brightness than that of the observed 308 μm transition of OH^+. With the lower limit of its formation, Table 9 shows that the 7166 GHz (42 μm) transition is below and the 6167 GHz (48 μm) transition is comparable to the observed 308 μm transition of OH^+. However, the optical depths of the 2076 and 3110 GHz transitions are found to be <1 with the lower limit. But the 2076 GHz transition is very much affected by the atmospheric transmission as shown in Figure 13(b), which calls into question its detectability.

In the case of HeH^+, we found that the optical depths of all transitions are <1. But, Figure 13(c) shows that only three transitions are showing a stronger surface brightness compared to the 308 μm transition of OH^+. Among them, the 2010 GHz (149 μm) transition is heavily affected by atmospheric transmission. The other two transitions at 4008 GHz (75 μm)

Table 8
Comparison between the Observed and Our Modeling Results

Atomic Lines	Flux (erg cm^{-2} s^{-1})		Predicted/Observed Ratio[a]	Predicted/Observed Ratio		
	Observed	Dereddened		Model A1	Model A2	Model B
H_2 λ2.12 μm	6.5×10^{-15}[a] (4.05×10^{-15})[b]	7.6×10^{-15}[a]	1.1[a]	5.3×10^{-4} (8.5×10^{-4})[c]	0.080 (0.127)[c]	0.022 (0.036)[c]
O II λ3727	7.7×10^{-14}[a]	6.7×10^{-13}[a]	1.0[a]	0.17	0.005	1.053
Ne III λ3869	1.7×10^{-14}[a]	1.4×10^{-13}[a]	1.1[a]	0.004	1.7×10^{-4}	1.144
H I λ4340	4.4×10^{-15}[a]	2.9×10^{-14}[a]	2.0[a]	20.728	16.056	4.330
He I λ4471	1.7×10^{-15}[a]	1.0×10^{-14}[a]	1.2[a]	187.452	189.495	13.029
He II λ4686	2.9×10^{-15}[a]	1.7×10^{-14}[a]	1.2[a]	1.697	0.965	1.013
H I λ4861	1.04×10^{-14}[a]	5.4×10^{-14}[a]	2.3[a]	18.826	14.675	3.931
O III λ5007	7.6×10^{-14}[a]	3.7×10^{-13}[a]	1.2[a]	1.8×10^{-5}	1.13×10^{-6}	0.958
N I λ5198	1.8×10^{-15}[a]	8.1×10^{-15}[a]	1.6[a]	7.261	1.096	1.301
He I λ5876	6.8×10^{-15}[a]	2.5×10^{-14}[a]	1.6[a]	125.885	128.481	8.751
O I λ6300	5.3×10^{-14}[a]	1.8×10^{-13}[a]	0.7[a]	7.120	0.981	0.357
H I λ6563	5.0×10^{-14}[a]	1.6×10^{-13}[a]	2.5[a]	11.400	9.020	2.384
N II λ6584	9.7×10^{-14}[a]	3.1×10^{-13}[a]	0.5[a]	0.357	0.029	0.296
S II λ6716	9.0×10^{-14}[a]	2.8×10^{-13}[a]	0.8[a]	...	...	0.468
S II λ6731	1.2×10^{-13}[a]	3.6×10^{-13}[a]	0.9[a]	...	...	0.582
He I λ7065	2.6×10^{-15}[a]	7.6×10^{-15}[a]	1.3[a]	204.777	200.769	10.875
Ar III λ7136	1.3×10^{-14}[a]	3.7×10^{-14}[a]	1.0[a]	0.285	0.026	0.542
Fe II λ7155	2.7×10^{-15}[a]	7.6×10^{-15}[a]	2.0[a]	...	...	1.608
O II λ7320	3.6×10^{-15}[a]	9.7×10^{-15}[a]	2.3[a]	0.017	1.3×10^{-4}	0.849
O III (52 μm)	4.2×10^{-15}[d]	...	...	0.001	7.3×10^{-4}	1.629
N III (57 μm)	4.0×10^{-16}[d]	...	...	3.0×10^{-4}	1.1×10^{-4}	1.610
O I (63 μm)	1.7×10^{-15}[d]	...	...	1089.851	1651.994	109.574
O III (88 μm)	3.6×10^{-15}[d]	...	...	2.1×10^{-4}	1.2×10^{-4}	0.613
N II (122 μm)	1.2×10^{-16}[d]	...	...	9.104	4.311	1.451
O I (145 μm)	8.0×10^{-17}[d]	...	...	1742.984	2981.480	83.172
C II (158 μm)	2.9×10^{-16}[d]	...	...	742.966	877.732	16.426

Notes.
[a] Richardson et al. (2013).
[b] Loh et al. (2011).
[c] Taking the ratio with the observed values of Loh et al. (2011).
[d] Gomez et al. (2012).

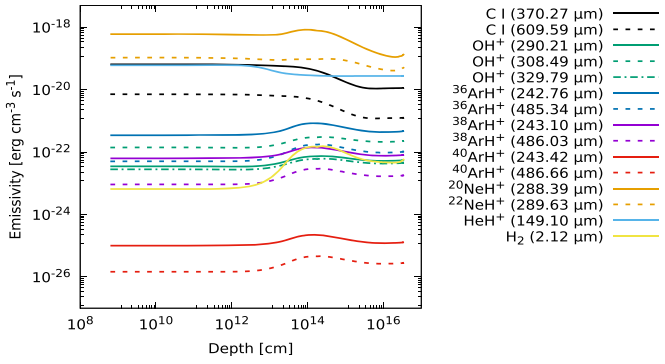

Figure 11. Emissivity of some of the strongest transitions that fall in the range of the frequency limit of Herschel's SPIRE and PACS spectrometer, and SOFIA with respect to the depth into the filament by considering $n_H = 2.00 \times 10^4$ cm^{-3} and $\zeta/\zeta_0 = 9.07 \times 10^6$ (Model A1).

and 5984 GHz (50 μm) are free from atmospheric features and produce a strong surface brightness.

Table 9 depicts that even with the upper limit of the formation, the surface brightness of all the transitions of XOH^+ (X = ^{36}Ar, ^{20}Ne, and He) is less than the surface brightness of the 308 μm transition of OH^+, so their chance of detection in the Crab environment is very difficult, and thus, we did not carry out any similar analysis for them.

4.2.2. Comparison with Observations: Model B

In Table 8, we have compared our obtained values with the observational (Loh et al. 2011, 2012; Gomez et al. 2012; Richardson et al. 2013; Priestley et al. 2017) as well as with the previous modeling results (Richardson et al. 2013). Though in Model B we have used similar parameters as used in Richardson et al. (2013), we obtained very little difference. This small difference is due to the changes in the associative detachment reactions between Cloudy version 10.00 (Ferland et al. 1998; used in Richardson et al. 2013) and version 17.02 (used in this work). In case of Model A, we did not obtain any transition of sulfur (S) and iron (Fe), because for this case, we did not consider any initial elemental abundance for these two elements (see Table 2). For Model A, we considered $n_H = 2.00 \times 10^4$ cm^{-3} and $\zeta/\zeta_0 = 9.07 \times 10^6$ (Model A1) and $n_H = 3.16 \times 10^4$ cm^{-3} and $\zeta/\zeta_0 = 4.55 \times 10^6$ (Model A2), whereas for Model B, we considered the ionizing particle model of Richardson et al. (2013), which yields a core density $n_{H(core)} = 10^{5.25}$ cm^{-3} and $\zeta/\zeta_0 = 7.06 \times 10^6$. The striking differences between Model A and Model B is the consideration of a very high abundance of He and a dust to gas ratio of 0.027 in Model A, whereas in Model B, by considering the initial elemental abundance pointed out in Table 2, we obtained (from the Cloudy output) a dust-to-gas mass ratio ~8 times lower than that of Model A. In Table 10, we provide H_2 vibrational line surface brightnesses relative to the 1–0 S(1) line for knot

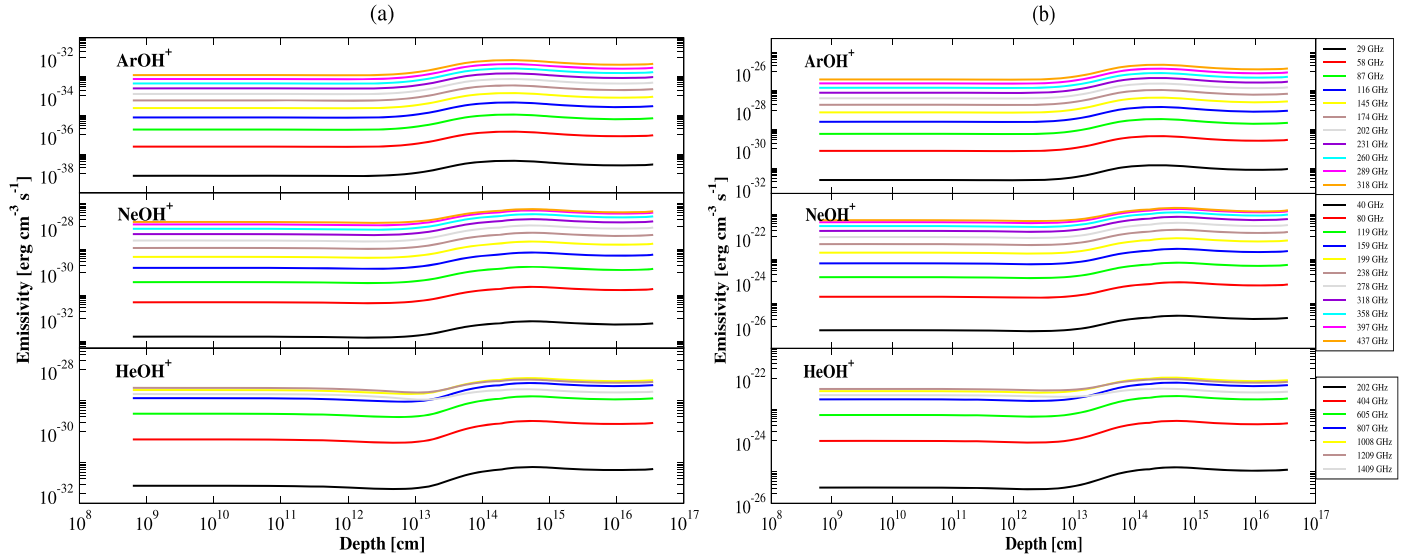

Figure 12. Calculated emissivity of various XOH^+ transitions (X = ^{36}Ar, ^{20}Ne, He) noted in Table 9 lying in the frequency limit of Herschel's SPIRE and PACS spectrometer, SOFIA, ALMA, VLA, IRAM 30 m, and NOEMA by considering $n_H = 2.00 \times 10^4\,cm^{-3}$ and $\zeta/\zeta_0 = 9.07 \times 10^6$ (Model A1). (a) Emissivity considering the formation rates following Bates (1983) mentioned in Section 3.3, whereas (b) considers the upper limit of $\sim 10^{-10}\,cm^3\,s^{-1}$.

51 for both of our Model A and Model B and compared with the observed values (Loh et al. 2012). We found that our Model A1 is able to reproduce the observed line strength ratio except the 2–1 S(X) (X = 1, 2, 3) lines, whereas our Model A2 and Model B are efficient enough to reproduce the 2–1 S(X) lines. All results obtained with Model B are shown in Appendix C (see Figures C1–C6).

4.3. Timescales of Molecule Formation

Richardson et al. (2013) and Priestley et al. (2017) mentioned that steady-state chemistry might not be applicable because of the H_2 formation timescale and mass-loss rate of the Crab knot. Richardson et al. (2013) used Cloudy version 10 for their study and Priestley et al. (2017) used the UCL PDR code (Bell et al. 2005, 2006; Bayet et al. 2011) for their study. Here, we used Cloudy version 17.02. Currently, to check whether the computation is time steady or not, we ran our model with the "*age*" command available in the Cloudy code. This command checks whether the microphysics is time steady or not. We found that both of our best-fitted models show that the longest timescale is below the age of the Cloud (for the best-fitted case of Model A, it is ∼9 yr and for Model B it is ∼134 yr). Thus, we are not overestimating the abundance of H_2 by considering the radiative attachment of H and then the associative detachment reaction. Because a time-dependent simulation is out of scope for this paper, we discuss here the timescale of their formation relevant to the environment of the Crab.

4.3.1. ArH^+

ArH^+ is mainly formed by the reaction between Ar^+ and H_2 (Priestley et al. 2017 also reported a similar observation) with a rate coefficient of $\sim 10^{-9}\,cm^3\,s^{-1}$. This yields a time of $\sim 10^9$ s ∼ 30 yr (sufficiently smaller than the age of the Crab) by considering a H_2 density $\sim 1\,cm^{-3}$. Our best-fitted zone is also within the limit of the observed surface brightness of H_2. In the observed region, we have a H_2 number density of $< 1\,cm^{-3}$. This rules out the overestimation of the formation of ArH^+ considered here. Our obtained intrinsic absolute line surface brightness and line surface brightness ratio match the observations.

4.3.2. NeH^+

In the case of NeH^+ formation, if we include the reaction between Ne^+ and H_2 (Ne chemistry reaction 5a; see Table 3) in our network, that controls the formation. By considering a H_2 number density of $\sim 1\,cm^{-3}$, the formation timescale is well within the age of the Crab as discussed in the context of ArH^+. However, in the absence of this pathway, we found that its formation depends on the HeH^+ + Ne route (Ne chemistry reaction 14). The rate coefficient for the reaction is $\sim 10^{-9}\,cm^3\,s^{-1}$. Because the number density of Ne is $\sim 1\,cm^{-3}$, it is very fast. However, its formation depends on HeH^+, which is produced by a comparatively slower process than ArH^+.

4.3.3. HeH^+

In the best-fitted model, the dominant pathway for the formation of HeH^+ is the reaction between He^+ and H. Priestley et al. (2017) also found this pathway to be the dominant one in their network. The rate coefficient used for this reaction is $\sim 1.44 \times 10^{-16}\,cm^3\,s^{-1}$ (Güsten et al. 2019 found the best fit with a rate constant of $\sim 6 \times 10^{-16}\,cm^3\,s^{-1}$). By considering the H density of $\sim 10^3$–$10^5\,cm^{-3}$ used here, the timescale for the formation of HeH^+ seems to be much slower ($\sim 10^3$ yr by considering the lowest He^+ abundance) than that of the ArH^+. However, it is possible to form HeH^+ within the lifetime of the Crab. The recent observation of HeH^+ in NGC 7027 (age of ∼600 yr) by Güsten et al. (2019) might be a strong reason to look for HeH^+ in the Crab.

Looking at the formation timescales of the hydride ions, it is quite possible that all these molecules will be likely spotted in the filamentary region of the Crab.

Table 9

Strongest Transitions Falling in the Range of Herschel's SPIRE and PACS Spectrometer, SOFIA, ALMA, VLA, IRAM 30 m, and NOEMA Considering $n_{\rm H} = 2.00 \times 10^4$ cm^{-3} and $\zeta/\zeta_0 = 9.07 \times 10^6$ (Model A1)

Species	Transitions	E_U (K)	Frequency (GHz) (μm)	Total Column Density (cm^{-2})	Optical Depth (τ)	Surface Brightness (erg cm^{-2} s^{-1} sr^{-1})
$^{36}ArH^+$	$J = 1 \rightarrow 0$	29.64	617.52 (485.34)	3.80×10^{11}	2.557×10^{-2}	2.84×10^{-7} ($(2.2 - 9.9) \times 10^{-7}$)[a]
$^{36}ArH^+$	$J = 2 \rightarrow 1$	88.89	1234.60 (242.76)	3.80×10^{11}	7.547×10^{-3}	1.29×10^{-6} ($(1.0 - 3.8) \times 10^{-6}$)[a]
$^{36}ArH^+$	J = 3 → 2	177.71	1850.78 (161.94)	3.80×10^{11}	4.258×10^{-4}	1.15×10^{-6}
$^{36}ArH^+$	$J = 4 \rightarrow 3$	296.04	2465.62 (121.56)	3.80×10^{11}	5.405×10^{-5}	7.76×10^{-7}
$^{36}ArH^+$	$J = 5 \rightarrow 4$	443.80	3078.68 (97.35)	3.80×10^{11}	1.287×10^{-5}	3.86×10^{-7}
$^{36}ArH^+$	$J = 6 \rightarrow 5$	620.86	3689.50 (81.23)	3.80×10^{11}	1.203×10^{-6}	8.63×10^{-8}
$^{36}ArH^+$	$J = 7 \rightarrow 6$	827.12	4297.65 (69.74)	3.80×10^{11}	4.792×10^{-8}	1.32×10^{-8}
$^{38}ArH^+$	$J = 1 \rightarrow 0$	29.39	616.65 (486.03)	6.57×10^{10}	4.431×10^{-3}	4.92×10^{-8}
$^{38}ArH^+$	$J = 2 \rightarrow 1$	88.14	1232.85 (243.10)	6.57×10^{10}	1.297×10^{-3}	2.24×10^{-7}
$^{38}ArH^+$	$J = 3 \rightarrow 2$	176.23	1848.16 (162.17)	6.57×10^{10}	7.320×10^{-5}	2.00×10^{-7}
$^{38}ArH^+$	$J = 4 \rightarrow 3$	293.57	2462.13 (121.73)	6.57×10^{10}	9.492×10^{-6}	1.36×10^{-7}
$^{38}ArH^+$	$J = 5 \rightarrow 4$	440.09	3074.32 (97.49)	6.57×10^{10}	2.255×10^{-6}	6.76×10^{-8}
$^{38}ArH^+$	$J = 6 \rightarrow 5$	615.68	3684.29 (81.35)	6.57×10^{10}	2.080×10^{-7}	1.50×10^{-8}
$^{38}ArH^+$	$J = 7 \rightarrow 6$	820.22	4291.58 (69.84)	6.57×10^{10}	8.343×10^{-9}	2.33×10^{-9}
$^{40}ArH^+$	$J = 1 \rightarrow 0$	29.35	615.86 (486.66)	1.04×10^{8}	7.012×10^{-6}	7.76×10^{-11}
$^{40}ArH^+$	$J = 2 \rightarrow 1$	88.03	1231.27 (243.42)	1.04×10^{8}	2.061×10^{-6}	3.35×10^{-10}
$^{40}ArH^+$	$J = 3 \rightarrow 2$	176.00	1845.79 (162.38)	1.04×10^{8}	1.160×10^{-7}	3.17×10^{-10}
$^{40}ArH^+$	$J = 4 \rightarrow 3$	293.20	2458.98 (121.88)	1.04×10^{8}	1.516×10^{-8}	2.15×10^{-10}
$^{40}ArH^+$	$J = 5 \rightarrow 4$	439.53	3070.39 (97.61)	1.04×10^{8}	3.578×10^{-9}	1.07×10^{-10}
$^{40}ArH^+$	$J = 6 \rightarrow 5$	614.890	3679.58 (81.45)	1.04×10^{8}	3.328×10^{-10}	2.38×10^{-11}
$^{40}ArH^+$	$J = 7 \rightarrow 6$	819.17	4286.11 (69.93)	1.04×10^{8}	1.323×10^{-11}	3.71×10^{-12}
$^{20}NeH^+$	$J = 1 \rightarrow 0$	49.53	1039.26 (288.39)	6.51×10^{14} (1.16×10^{13})[b]	4.246×10^{1} (2.175)[b]	4.20×10^{-4} (3.97×10^{-5})[b]
$^{20}NeH^+$	$J = 2 \rightarrow 1$	148.50	2076.57 (144.33)	6.51×10^{14} (1.16×10^{13})[b]	4.022×10^{1} (1.352×10^{-1})[b]	2.41×10^{-3} (6.74×10^{-5})[b]
$^{20}NeH^+$	$J = 3 \rightarrow 2$	296.72	3110.02 (96.37)	6.51×10^{14} (1.16×10^{13})[b]	4.794 (2.352×10^{-3})[b]	3.67×10^{-3} (4.95×10^{-5})[b]
$^{20}NeH^+$	$J = 4 \rightarrow 3$	493.92	4137.67 (72.43)	6.51×10^{14} (1.16×10^{13})[b]	8.114×10^{-2} (3.061×10^{-4})[b]	2.40×10^{-3} (3.44×10^{-5})[b]
$^{20}NeH^+$	$J = 5 \rightarrow 4$	739.73	5157.61 (58.11)	6.51×10^{14} (1.16×10^{13})[b]	4.225×10^{-3} (8.033×10^{-5})[b]	1.26×10^{-3} (9.92×10^{-6})[b]
$^{20}NeH^+$	$J = 6 \rightarrow 5$	1033.68	6167.92 (48.59)	6.51×10^{14} (1.16×10^{13})[b]	6.559×10^{-4} (2.499×10^{-6})[b]	4.36×10^{-4} (7.74×10^{-7})[b]
$^{20}NeH^+$	$J = 7 \rightarrow 6$	1375.24	7166.70 (41.82)	6.51×10^{14} (1.16×10^{13})[b]	3.649×10^{-5} (4.035×10^{-8})[b]	5.49×10^{-5} (6.29×10^{-8})[b]
$^{22}NeH^+$	$J = 1 \rightarrow 0$	49.32	1034.79(289.63)	5.94×10^{13}	8.939	1.34×10^{-4}
$^{22}NeH^+$	$J = 2 \rightarrow 1$	147.86	2067.67 (144.95)	5.94×10^{13}	1.771	4.00×10^{-4}
$^{22}NeH^+$	$J = 3 \rightarrow 2$	295.45	3096.70 (96.78)	5.94×10^{13}	2.453×10^{-2}	3.11×10^{-4}
$^{22}NeH^+$	$J = 4 \rightarrow 3$	491.80	4119.99 (72.74)	5.94×10^{13}	1.659×10^{-3}	2.05×10^{-4}
$^{22}NeH^+$	$J = 5 \rightarrow 4$	736.56	5135.64 (58.36)	5.94×10^{13}	4.031×10^{-4}	8.45×10^{-5}
$^{22}NeH^+$	$J = 6 \rightarrow 5$	1029.28	6141.73 (48.80)	5.94×10^{13}	2.677×10^{-5}	1.08×10^{-5}
$^{22}NeH^+$	$J = 7 \rightarrow 6$	1369.39	7136.41 (41.99)	5.94×10^{13}	4.307×10^{-7}	7.22×10^{-7}
HeH^+	J = 1 → 0	95.80	2010.18 (149.10)	1.33×10^{13}	8.473×10^{-1}	7.68×10^{-5}
HeH^+	$J = 2 \rightarrow 1$	286.86	4008.73 (74.76)	1.33×10^{13}	7.901×10^{-3}	6.51×10^{-5}
HeH^+	$J = 3 \rightarrow 2$	572.06	5984.14 (50.08)	1.33×10^{13}	2.080×10^{-4}	6.69×10^{-6}
HeH^+	$J = 4 \rightarrow 3$	949.76	7925.15 (37.82)	1.33×10^{13}	1.454×10^{-6}	3.18×10^{-7}
HeH^+	$J = 5 \rightarrow 4$	1417.82	9820.88 (30.52)	1.33×10^{13}	1.289×10^{-8}	1.22×10^{-8}
HeH^+	$J = 6 \rightarrow 5$	1973.57	11660.90 (25.70)	1.33×10^{13}	7.291×10^{-11}	2.77×10^{-9}
HeH^+	$J = 7 \rightarrow 6$	2613.89	13435.35 (22.31)	1.33×10^{13}	1.356×10^{-12}	1.47×10^{-9}
OH^+	$J = 2 \rightarrow 1$ (F = 5/2 → 3/2)	46.64	971.80 (308.41)	6.53×10^{11}	2.370×10^{-2}	6.17×10^{-7} ($(3.4 - 10.3) \times 10^{-7}$)[a]

Table 9
(Continued)

Species	Transitions	E_U (K)	Frequency (GHz) (μm)	Total Column Density (cm^{-2})	Optical Depth (τ)	Surface Brightness (erg cm^{-2} s^{-1} sr^{-1})
$^{36}ArOH^+$	$J = 1 \rightarrow 0$ ($K_- = 1 \rightarrow 0$)	1.38	28.94 (10358)	6.19×10^{10}	6.617×10^{-10}	7.76×10^{-23}
$^{36}ArOH^+$	$J = 2 \rightarrow 1$ ($K_- = 2 \rightarrow 1$)	4.14	57.88 (5179)	6.19×10^{10}	2.740×10^{-9}	2.48×10^{-21}
$^{36}ArOH^+$	$J = 3 \rightarrow 2$ ($K_- = 3 \rightarrow 2$)	8.28	86.82 (3453)	6.19×10^{10}	6.561×10^{-9}	1.88×10^{-20}
$^{36}ArOH^+$	$J = 4 \rightarrow 3$ ($K_- = 4 \rightarrow 3$)	13.79	115.76 (2590)	6.19×10^{10}	1.225×10^{-8}	7.91×10^{-20}
$^{36}ArOH^+$	$J = 5 \rightarrow 4$ ($K_- = 5 \rightarrow 4$)	20.69	144.70 (2072)	6.19×10^{10}	2.183×10^{-8}	2.41×10^{-19}
$^{36}ArOH^+$	$J = 6 \rightarrow 5$ ($K_- = 6 \rightarrow 5$)	28.96	173.63 (1727)	6.19×10^{10}	3.602×10^{-8}	5.97×10^{-19}
$^{36}ArOH^+$	$J = 7 \rightarrow 6$ ($K_- = 7 \rightarrow 6$)	38.62	202.56 (1480)	6.19×10^{10}	5.809×10^{-8}	1.29×10^{-18}
$^{36}ArOH^+$	$J = 8 \rightarrow 7$ ($K_- = 8 \rightarrow 7$)	49.65	231.48 (1295)	6.19×10^{10}	5.900×10^{-8}	2.50×10^{-18}
$^{36}ArOH^+$	$J = 9 \rightarrow 8$ ($K_- = 9 \rightarrow 8$)	62.06	260.40 (1151)	6.19×10^{10}	1.088×10^{-7}	4.49×10^{-18}
$^{36}ArOH^+$	$J = 10 \rightarrow 9$ ($K_- = 10 \rightarrow 9$)	75.85	289.32 (1036)	6.19×10^{10}	1.845×10^{-7}	7.57×10^{-18}
$^{36}ArOH^+$	$J = 11 \rightarrow 10$ ($K_- = 11 \rightarrow 10$)	91.02	318.22 (942)	6.19×10^{10}	4.923×10^{-7}	1.21×10^{-17}
$^{20}NeOH^+$	$J = 1 \rightarrow 0$ ($K_- = 1 \rightarrow 0$)	1.89	39.76 (7540)	1.02×10^{14}	...	1.56×10^{-17}
$^{20}NeOH^+$	$J = 2 \rightarrow 1$ ($K_- = 2 \rightarrow 1$)	5.68	79.52 (3770)	1.02×10^{14}	...	4.97×10^{-16}
$^{20}NeOH^+$	$J = 3 \rightarrow 2$ ($K_- = 3 \rightarrow 2$)	11.37	119.27 (2514)	1.02×10^{14}	3.914×10^{-3}	3.78×10^{-15}
$^{20}NeOH^+$	$J = 4 \rightarrow 3$ ($K_- = 4 \rightarrow 3$)	18.95	159.01 (1885)	1.02×10^{14}	1.895×10^{-2}	1.58×10^{-14}
$^{20}NeOH^+$	$J = 5 \rightarrow 4$ ($K_- = 5 \rightarrow 4$)	28.42	198.75 (1508)	1.02×10^{14}	5.306×10^{-2}	4.77×10^{-14}
$^{20}NeOH^+$	$J = 6 \rightarrow 5$ ($K_- = 6 \rightarrow 5$)	39.78	238.47 (1257)	1.02×10^{14}	1.047×10^{-1}	1.16×10^{-13}
$^{20}NeOH^+$	$J = 7 \rightarrow 6$ ($K_- = 7 \rightarrow 6$)	53.04	278.18 (1078)	1.02×10^{14}	1.603×10^{-1}	2.41×10^{-13}
$^{20}NeOH^+$	$J = 8 \rightarrow 7$ ($K_- = 8 \rightarrow 7$)	68.19	317.88 (943)	1.02×10^{14}	1.998×10^{-1}	4.52×10^{-13}
$^{20}NeOH^+$	$J = 9 \rightarrow 8$ ($K_- = 9 \rightarrow 8$)	85.23	357.56 (838)	1.02×10^{14}	2.322×10^{-1}	7.46×10^{-13}
$^{20}NeOH^+$	$J = 10 \rightarrow 9$ ($K_- = 10 \rightarrow 9$)	104.16	397.21 (755)	1.02×10^{14}	2.176×10^{-1}	1.09×10^{-12}
$^{20}NeOH^+$	$J = 11 \rightarrow 10$ ($K_- = 11 \rightarrow 10$)	124.98	436.84 (686)	1.02×10^{14}	1.674×10^{-1}	1.24×10^{-12}
$HeOH^+$	$J = 1 \rightarrow 0$ ($K_- = 1 \rightarrow 0$)	9.62	201.89 (1485)	8.19×10^{11}	...	1.67×10^{-16}
$HeOH^+$	$J = 2 \rightarrow 1$ ($K_- = 2 \rightarrow 1$)	28.86	403.71 (742)	8.19×10^{11}	1.013×10^{-3}	5.12×10^{-15}
$HeOH^+$	$J = 3 \rightarrow 2$ ($K_- = 3 \rightarrow 2$)	57.71	605.39 (495)	8.19×10^{11}	2.158×10^{-3}	3.19×10^{-14}
$HeOH^+$	$J = 4 \rightarrow 3$ ($K_- = 4 \rightarrow 3$)	96.17	806.85 (372)	8.19×10^{11}	1.330×10^{-3}	8.53×10^{-14}
$HeOH^+$	$J = 5 \rightarrow 4$ ($K_- = 5 \rightarrow 4$)	144.21	1008.02 (297)	8.19×10^{11}	4.246×10^{-4}	1.23×10^{-13}
$HeOH^+$	$J = 6 \rightarrow 5$ ($K_- = 6 \rightarrow 5$)	201.82	1208.84 (248)	8.19×10^{11}	8.820×10^{-5}	1.09×10^{-13}
$HeOH^+$	$J = 7 \rightarrow 6$ ($K_- = 7 \rightarrow 6$)	268.98	1409.22 (213)	8.19×10^{11}	1.331×10^{-5}	5.30×10^{-14}

Notes.
[a] Barlow et al. (2013).
[b] The total column density, optical depth, and surface brightness of $^{20}NeH^+$ transitions are also provided in the parentheses when reaction 5a of the Ne chemistry network is off, Hydride cations of noble gases and OH^+ are calculated using the lower limit of the formation rate, whereas hydroxyl cations of noble gases are calculated using the upper limit of the formation rate mentioned in Section 3.3. Following Bates's (1983) formation rate, the total column density of the hydroxyl cations of noble gases are $ArOH^+ = 1.97 \times 10^4$ cm^{-2}, $NeOH^+ = 2.59 \times 10^7$ cm^{-2}, and $HeOH^+ = 4.34 \times 10^5$ cm^{-2}.

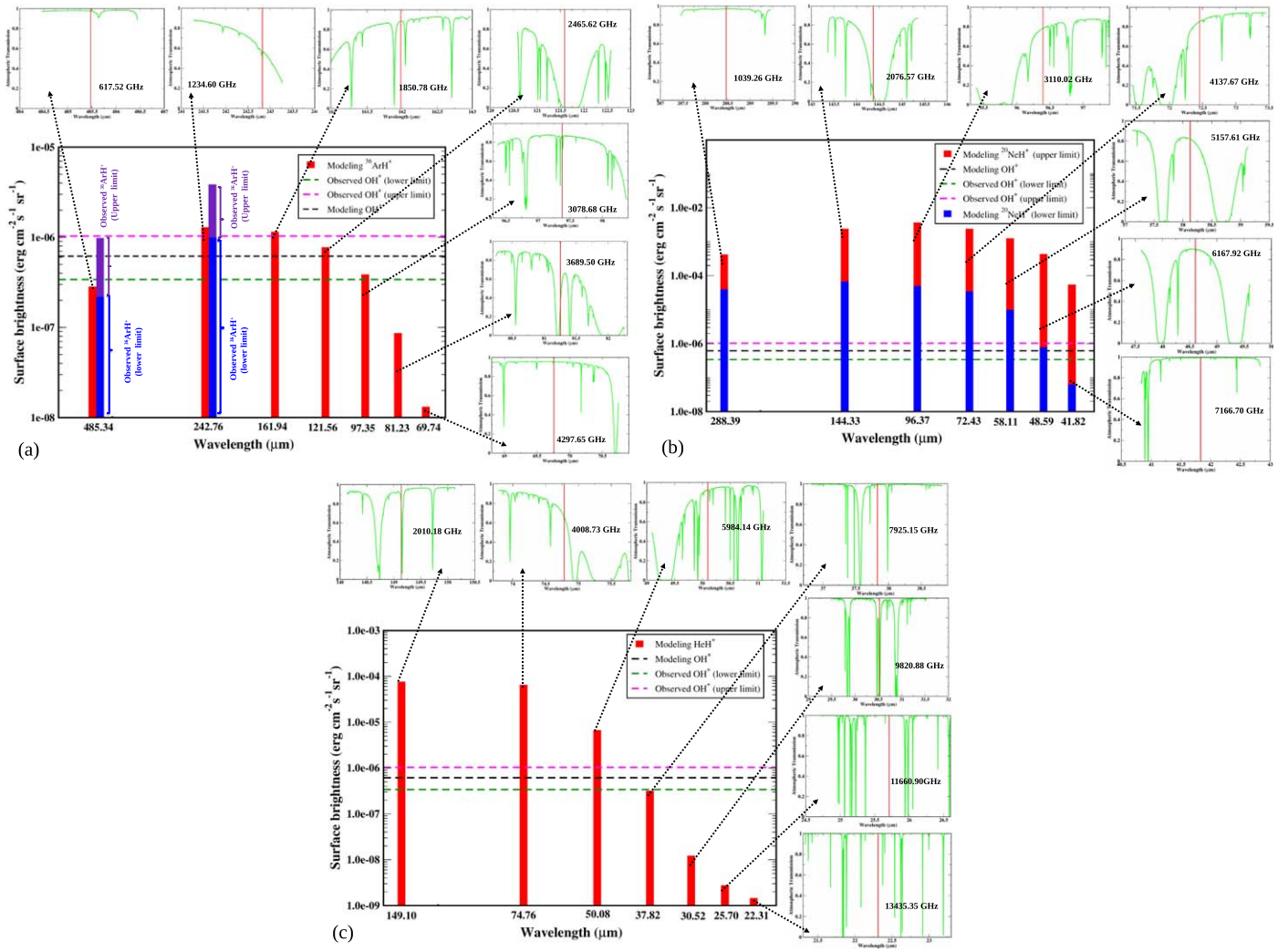

Figure 13. Comparison between the observed surface brightness of the 308 μm transition of OH^+ and the transitions of (a) $^{36}ArH^+$, (b) $^{20}NeH^+$, and (c) HeH^+ is shown. The atmospheric transmission for each transition is shown to check the fate of their identification.

Table 10
H_2 Vibrational Line Surface Brightnesses (SB) Relative to the 1–0 S(1) Line for Knot 51 from Loh et al. (2012) and for Our Final Models

H_2 Lines	Wavelength (μm)	SB (erg cm^{-2} s^{-1} sr^{-1})			SB Relative to the 1–0 S(1) Line			Observed SB Relative to the 1–0 S(1) Line for Knot 51
		Model A1	Model A2	Model B	Model A1	Model A2	Model B	
1–0 S(0)	2.22269	3.13×10^{-8}	4.38×10^{-6}	1.24×10^{-6}	0.214	0.200	0.200	0.23 ± 0.04[a]
1–0 S(1)	2.12125	1.46×10^{-7}	2.18×10^{-5}	6.18×10^{-6}	1.000	1.000	1.000	1 ± 0.04[a]
1–0 S(2)	2.03320	7.50×10^{-8}	9.35×10^{-6}	2.69×10^{-6}	0.513	0.428	0.436	0.52 ± 0.09[a]
2–1 S(1)	2.24711	1.17×10^{-7}	5.47×10^{-6}	1.49×10^{-6}	0.798	0.251	0.242	0.19 ± 0.03[a]
2–1 S(2)	2.15364	6.25×10^{-8}	2.40×10^{-6}	6.64×10^{-7}	0.428	0.110	0.107	<0.13[a]
2–1 S(3)	2.07294	1.90×10^{-7}	7.31×10^{-6}	1.97×10^{-6}	1.300	0.335	0.319	<0.28[a]

Note.
[a] Loh et al. (2012).

4.3.4. $ArOH^+$, $NeOH^+$, and $HeOH^+$

These three noble gas hydroxyl cations are mainly formed in our network by radiative association reactions (see Section 3.3). The rate coefficients of these reactions are calculated by using a temperature-independent semiempirical formula proposed by Bates (1983). This yielded a very slow rate of formation and thus very unlikely to be formed in the Crab environment. However, the formula provided by Bates (1983) to calculate the rate coefficients is temperature-independent and was approximated for the temperature of ~30 K. In the condition relevant to the Crab (temperature ~2000–3000 K), this semiempirical relation might underestimate the rate. To have an educated estimation of their formation, we considered an upper limit of these rates ($\sim 10^{-10}$ cm^3 s^{-1}). In the case of $ArOH^+$ and $NeOH^+$ formation, the dominant pathway in our network is the reaction between ArH^+ and O and NeH^+ and O respectively (reaction 13; see

Table 3). For $HeOH^+$ formation, the reaction between He^+ and OH dominates (reaction 12 of He chemistry network). Due to this reason, the $ArOH^+$ and $NeOH^+$ abundance profiles follow the ArH^+ and NeH^+ abundance profiles. respectively, whereas $HeOH^+$ roughly follows the abundance profile of OH. We noticed that only with the upper limit of the formation, the abundances of these species are significant. Otherwise, the formation timescale is much slower and thus very unlikely to be formed in the Crab environment. But the pathways proposed here are very useful to study their formation in other sources where they have a much longer time for their formation.

5. Conclusions

The detection of ArH^+ ions in the Crab filament inspired us to study the presence of other hydride and hydroxyl cations in the same environment. Moreover, to check the detectability of other noble gas hydride and hydroxyl cations, we modeled a Crab filament using the spectral synthesis code, Cloudy. A wide range of parameter space was used to suitably explain the observational aspects. We have checked that under the conditions of the Crab Nebula, using steady-state chemistry is justified for our best-fitted models. Our findings are highlighted below:

1. We prepared a realistic chemical network to study the chemical evolution of the hydride and hydroxyl cations of the various isotopes of Ar, Ne, and He. We did not consider any fractionation reactions between the isotopologs. We found that the abundances of $^{36}ArH^+$, $^{20}NeH^+$, and HeH^+ are comparable to the abundance of OH^+ in the Crab filament. Considering the upper limit of the formation rate, we obtained reasonably high abundances of $^{36}ArOH^+$, $^{20}NeOH^+$, and $HeOH^+$. However, using the realistic rates of these reactions, we obtained very low abundances of these hydroxyl ions. It is thus important to accurately measure/estimate these rates.
2. In the diffuse ISM, we found that the XH^+ (X = Ar, Ne, and He) fractional abundance is reasonably high and could have been identified. For example, we found a peak fractional abundance of $\sim 1.3 \times 10^{-9}$ for $^{36}ArH^+$. $^{20}NeH^+$ seems to be also highly abundant (peak abundance $\sim 5 \times 10^{-8}$) when reaction 5a ($Ne^+ + H_2 \rightarrow NeH^+ + H$) of the Ne chemistry is considered. However, its peak fractional abundance significantly drops ($\sim 3 \times 10^{-11}$) in the absence of this pathway. We obtained the peak fractional abundance of $HeH^+ \sim 3 \times 10^{-11}$.
3. We found that a high value of the cosmic-ray ionization rate ($\zeta/\zeta_0 \sim 10^{6-7}$) with a total hydrogen density a few times 10^4–$10^6\,cm^{-3}$ can successfully reproduce the absolute surface brightness of the two transitions of $^{36}ArH^+$ (242 and 485 μm), the 308 μm transition of OH^+, and the 2.12 μm transition of H_2.
4. With favorable values of n_H and ζ/ζ_0, we are able to successfully explain the observed surface brightness ratio between (a) the 2−1 and 1−0 transitions of $^{36}ArH^+$, (b) two transitions (2−1 and 1−0) of $^{36}ArH^+$ and the 308 μm transition of OH^+, and (c) various transitions of CO with respect to the 308 μm transition of OH^+. Our most suitable case can explain the surface brightness ratio obtained by Priestley et al. (2017) between the transitions (a) HeH^+ and 146 μm of [O I], and (b) 3−2 and 2−1 of HeH^+. It can also explain the surface brightness ratio between the transitions (a) 63 μm and 146 μm of [O I], and (b) 146 μm of [O I] and 158 μm of [C II] observed by Gomez et al. (2012) using Herschel PACS and ISO Long Wavelength Spectrometer (LWS) fluxes for infrared fine-structure emission lines. However, our Model A always overproduces the surface brightness of [C I], and even around the low A_V region, we have the fractional abundance of CO and OH $\sim 10^{-11}$–10^{-9}. A major reason for this is the obtained electron temperature ($\sim$4000 K) with Model A. We found that our Model B requires a much higher electron temperature (>10000 K) to explain most of the observed features in the Crab filamentary region.
5. The optical depth of the most probable transitions of XH^+ and XOH^+ (where X = Ar, Ne, and He) were calculated for the Crab. Analyzing the obtained results, we noticed that the 485 μm, 242 μm, and 162 μm transitions of $^{36}ArH^+$; 96 μm, 72 μm, 58 μm, and 48 μm transitions of $^{20}NeH^+$; and 75 μm and 50 μm transitions of HeH^+ are most likely to be identified with a space-based observation. However, the fate of detecting XOH^+ in a similar environment with a similar facility is very difficult.
6. We calculated the ground vibrational and equilibrium values of rotational constants and asymmetrically reduced quartic centrifugal distortion constants for various isotopologs of $ArOH^+$ and $NeOH^+$, and compared them with the theoretically calculated values of Theis & Fortenberry (2016). We also provided these constants for $HeOH^+$, which was not available until now. Moreover, we provided the catalog files per JPL style for various isotopologs of $ArOH^+$ and $NeOH^+$ (with both the ground vibrational and equilibrium rotational constants of Theis & Fortenberry 2016), and $HeOH^+$ (with our calculated ground vibrational and equilibrium values), which might enable their future astronomical detection in other sources.

We thank the referee for fruitful comments and suggestions. A.D. wants to acknowledge ISRO respond (grant No. ISRO/RES/2/402/16-17). M.S. [IF160109] and B.B. [IF170046] gratefully acknowledge a DST-INSPIRE Fellowship scheme for financial assistance. P.G. acknowledges the support of CSIR (grant No. 09/904 (0013) 2K18 EMR-I) and Chalmers Cosmic Origins postdoctoral fellowship. This research was possible in part due to a grant-in-aid from the Higher Education Department of the Government of West Bengal. P.C. acknowledges the support of the Max Planck Society.

Software: Cloudy 17.02 (Ferland et al. 2017), Gaussian 09 (Frisch et al. 2013), RADEX (van der Tak et al. 2007), ATRAN (Lord 1992).

Appendix A
X-Ray Ionization

A.1. Direct X-Ray Ionization

In Table 3, we have pointed out the direct X-ray ionization rates in reaction numbers 25–26 for Ar, 26–27 for Ne, and 17–18 for He. Rate constants are computed using the method discussed in the following.

Table A1
Parameters Taken from Verner & Yakovlev (1995) for Calculating the Ionization Cross Sections $\sigma_i(E)$

Species	E_0 (eV)	σ_0 (cm^2)	y_a	P
He I	0.2024×10^1	0.2578×10^{-14}	0.9648×10^1	0.6218×10^1
Ne I	0.3144×10^3	0.1664×10^{-16}	0.2042×10^6	0.8450×10^0
Ar I	0.1135×10^4	0.4280×10^{-17}	0.3285×10^8	0.7631×10^0

We used the direct (or primary) ionization rate of species i at a certain depth z into the filament as:

$$\zeta_{\rm XR} = \zeta_{i,\rm prim} = \int_{E_{\rm min}}^{E_{\rm max}} \sigma_i(E) \frac{F(E, z)}{E} dE \ {\rm s}^{-1}, \quad \text{(A1)}$$

where the integration bound is the spectral range of the emitted energy ($[E_{\rm min}, E_{\rm max}] = [1, 10]$ keV (Meijerink & Spaans 2005) for the entire X-ray rate calculations). The ionization cross section $\sigma_i(E)$ at energy E is calculated by using Equations (A2) and (A3) and the parameters provided in Table A1. Verner & Yakovlev (1995) used a fitting procedure proposed by Kamrukov et al. (1983) for partial photoionization cross section $\sigma_{nl}(E)$ for different atoms and ions:

$$\sigma_i(E) = \sigma_{nl}(E) = \sigma_0 F(y), \ y = E/E_0, \quad \text{(A2)}$$

$$F(y) = [(y-1)^2 + y_w^2] y^{-Q} \left(1 + \sqrt{\frac{y}{y_a}}\right)^{-P},$$

$$Q = 5.5 + l - 0.5P, \quad \text{(A3)}$$

where n is the principal quantum number of the shell, $l = 0$, 1, 2 (or s, p, d) is the subshell orbital quantum number, E is the photon energy in eV, $\sigma_0 = \sigma_0$ (nl, Z, N), $E_0 = E_0(nl, Z, N)$, y_w, y_a, and P are the fitting parameters given in Table A1 (Z and N are the atomic number and number of electrons, respectively). Verner & Yakovlev (1995) noticed that $F(y)$ is a "nearly universal" function for all species (Z, N) at a fixed shell nl.

The flux $F(E, z)$ in Equation (A1) at depth z into the filament is given by

$$F(E, z) = F(E, z = 0) \exp(-\sigma_{\rm pa}(E) N_{\rm H}), \quad \text{(A4)}$$

where $N_{\rm H} \sim 4.77 \times 10^{21}$ cm^{-2} is considered as the total column density of hydrogen nuclei and $F(E, z = 0) = 0.35$ erg cm^{-2} s^{-1} is considered as the flux at the surface of the cloud. The photoelectric absorption cross section per hydrogen nucleus, $\sigma_{\rm pa}$, used in Equation (A4) is given by

$$\sigma_{\rm pa}(E) = \sum_i A_i({\rm total}) \sigma_i(E), \quad \text{(A5)}$$

where A_i(total) is the total (gas and dust) elemental abundance used.

A.2. Secondary X-Ray Ionization

Part of the kinetic energy of fast photoelectrons is lost by ionizations. These secondary ionizations are far more important for H, H_2, and He than direct ionization. The energy carried away by the fast photoelectrons and Auger electrons is very efficient in ionizing the other species. For example, these electrons can readily ionize H, He, and H_2 and decay back to ground state by the removal of UV photons. These photons can trigger the induced chemistry and are very important for the chemical network. The secondary ionization rate per hydrogen molecule at depth z into the filament can be calculated using

$$\zeta_{\rm H_2,XRPHOT} = \zeta_{i,\rm sec} = \int_{E_{\rm min}}^{E_{\rm max}} \sigma_{\rm pa}(E) F(E, z) \frac{E}{W x({\rm H_2})} dE \ {\rm s}^{-1}, \quad \text{(A6)}$$

where $x(H_2)$ is the fractional abundance of H_2 with respect to total hydrogen nuclei and W is the mean energy per ion pair. For our calculations, we considered $x(H_2) \sim 2 \times 10^{-4}$, which means that most of the hydrogen is in atomic form. Dalgarno et al. (1999) calculated W for pure ionized H–He and H_2–He mixtures for E between 30 eV and 1 keV and parameterized W as

$$W = W_0(1 + Cx^{\alpha}), \quad \text{(A7)}$$

where $x = 0.1$ is considered as the ionization fraction and W_0 is the value for neutral gas. W_0, C, and α are given in Table 4 of Dalgarno et al. (1999). We took those values ($W_0 = 48.6$ eV, $C = 9.13$, and $\alpha = 0.807$) only for pure He gas for 1 keV. Following Meijerink & Spaans (2005), we integrated over the range 1–10 keV and W goes to a limiting value (42.69 eV). We considered the parameters for the 1 keV electron to determine the electron energy deposition, because these parameters do not change for higher energies. The X-ray photoionization rate then simplifies to

$$\zeta_{\rm H_2,XRPHOT} = \zeta_{i,\rm sec} = \frac{1 \ {\rm keV}}{W(1 \ {\rm keV}) x({\rm H_2})} \int_{E_{\rm min}}^{E_{\rm max}} \sigma_{\rm pa}(E) F(E, z) dE \ {\rm s}^{-1}. \quad \text{(A8)}$$

The photon energy absorbed per hydrogen nucleus H_X is given by

$$H_X = \int_{E_{\rm min}}^{E_{\rm max}} \sigma_{\rm pa}(E) F(E, z) dE. \quad \text{(A9)}$$

Hence, the X-ray photoionization rate is given by

$$\zeta_{\rm H_2,XRPHOT} = \zeta_{i,\rm sec} = \frac{1 \ {\rm keV}}{W(1 \ {\rm keV}) x({\rm H_2})} H_X \ {\rm s}^{-1}. \quad \text{(A10)}$$

Following Priestley et al. (2017), we multiplied $\zeta_{\rm H_2,XRPHOT}$ by $\frac{0.8}{1-\omega}$, where ω is the grain albedo ($\sim$0.5).

A.3. Electron-impact X-Ray Ionization

The electron-impact ionization rate ($\zeta_{\rm XRSEC}$) of other atoms or molecules can be calculated as a first approximation by

$$\zeta_{\rm XRSEC} = \zeta_{\rm H_2,XRPHOT} \times R_\sigma, \quad \text{(A11)}$$

where R_σ is the ratio of electron-impact cross sections of that species to H_2 at a specific energy (Stäuber et al. 2005). For simplicity, here we assumed $\zeta_{\rm H2,XRPHOT} = \zeta_{\rm H,XRPHOT}$. Following Lennon et al. (1988), we determined the rate coefficients

Table A2
Parameters Taken from Lennon et al. (1988) to Calculate the Rate Coefficients $\langle \sigma v \rangle$

Parameters ($cm^3\ s^{-1}$)	Species			
	H I	He I	Ne I	Ar I
a_0	2.3743×10^{-08}	1.4999×10^{-08}	2.5262×10^{-08}	9.4727×10^{-08}
a_1	-3.6867×10^{-09}	5.6657×10^{-10}	1.6088×10^{-09}	1.4910×10^{-09}
a_2	-1.0366×10^{-08}	-6.0822×10^{-09}	1.5446×10^{-08}	-5.9294×10^{-08}
a_3	-3.8010×10^{-09}	-3.5594×10^{-09}	-3.5149×10^{-08}	1.7977×10^{08}
a_4	3.4159×10^{-09}	1.5529×10^{-09}	-1.0676×10^{-09}	1.2962×10^{-08}
a_5	1.6834×10^{-09}	1.3207×10^{-09}	1.2656×10^{-08}	-9.7203×10^{-09}
α	2.4617×10^{-08}	3.1373×10^{-08}	1.4653×10^{-07}	4.2289×10^{-07}
β_0	9.5987×10^{-08}	4.7094×10^{-08}	-1.8777×10^{-07}	-5.8297×10^{-07}
β_1	-9.2464×10^{-07}	-7.7361×10^{-07}	1.5661×10^{-08}	1.2344×10^{-06}
β_2	3.9974×10^{-06}	3.7367×10^{-06}	1.9135×10^{-06}	-7.2826×10^{-07}
$\langle \sigma v \rangle$	3.00×10^{-08}	2.53×10^{-08}	5.51×10^{-08}	1.66×10^{-07}

Table A3
Calculated Values of X-Ray Ionization Rates

Species	ζ_{XR} (s^{-1})	ζ_{XRPHOT} (s^{-1})	ζ_{XRSEC} (s^{-1})
^{36}Ar	3.85×10^{-13}	1.67×10^{-10}	5.79×10^{-10}
^{38}Ar	1.53×10^{-12}	3.31×10^{-10}	1.14×10^{-9}
^{40}Ar	1.35×10^{-11}	4.57×10^{-11}	1.58×10^{-10}
^{20}Ne	2.47×10^{-17}	8.28×10^{-15}	9.52×10^{-15}
^{22}Ne	9.41×10^{-15}	7.27×10^{-13}	8.36×10^{-13}
He	1.31×10^{-19}	1.67×10^{-14}	8.76×10^{-15}

$\langle \sigma v \rangle$ (cross sections at a given energy multiplied by electron velocity v at the same energy, evaluated over a Maxwellian velocity distribution) given by

$$\langle \sigma v \rangle = \left(\frac{8kT}{\pi m}\right)^{1/2} \int_{I/kT}^{\infty} \sigma(E) \left(\frac{E}{kT}\right) \exp\left(\frac{-E}{kT}\right) d\left(\frac{E}{kT}\right), \quad \text{(A12)}$$

where m is the electron mass. For the temperature range $I/10 \leqslant kT \leqslant 10I$, they fitted the rate coefficient with the following functional form,

$$\langle \sigma v \rangle = \exp\left(\frac{-I}{kT}\right)\left(\frac{kT}{I}\right)^{1/2} \sum_{n=0}^{5} a_n \left[\log_{10}\left(\frac{kT}{I}\right)\right]^n, \quad \text{(A13)}$$

and for $kT > 10I$, they used the formula

$$\langle \sigma v \rangle = \left(\frac{kT}{I}\right)^{-1/2} \left[\alpha \ln\left(\frac{kT}{I}\right) + \sum_{n=0}^{2} \beta_n \left(\frac{I}{kT}\right)^n\right]. \quad \text{(A14)}$$

Following Lennon et al. (1988), the coefficients a_0, ..., a_5 and α, β_0, β_1 and β_2 are given in Table A2. For T in K, I in eV, and $k = 0.8617 \times 10^{-4}$ eV K^{-1}, these coefficients provide the rate $\langle \sigma v \rangle$ in $cm^3\ s^{-1}$. Using Equations (A12) and (A13), we have determined $\langle \sigma v \rangle$ for Ar, Ne, and He. The obtained values are shown in the last row of Table A2 and the calculated values of R_σ are 5.53, 1.84, and 0.84 for Ar, Ne, and He, respectively. All of the calculated values of the different X-ray ionization rates of argon, neon, and helium are provided in Table A3.

Appendix B
Spectroscopic Information

Spectroscopic information of ArH^+, NeH^+, and HeH^+ is already available in the CDMS catalog. However, NeH^+ and HeH^+ are yet to be identified in the Crab environment. The $1 \rightarrow 0$ (2010.18 GHz) and $2 \rightarrow 1$ (4008.73 GHz) transitions of HeH^+ fall in the range of SOFIA and the PACS instrument of Herschel. The $1 \rightarrow 0$ transition of NeH^+ (1039.25 GHz) is well within the range of the SPIRE instrument of Herschel and of SOFIA, whereas the $2 \rightarrow 1$ transition of NeH^+ (2076.57 GHz) falls in the PACS and SOFIA limit. We prepared the collisional data files for NeH^+ and HeH^+ to study the observability of the transitions of the hydride ions. To prepare the collisional data file, we considered that electrons are the only colliding partners. We used the electron-impact excitation of HeH^+ from Hamilton et al. (2016) for this collisional data file. For NeH^+, no collisional rates were available, and thus we approximated the collisional rates of NeH^+ by considering the collisional rates of $ArH^+ - e^-$.

One of the aims of this paper is to study the emission line of hydroxyl ions of the noble gases. Recently, Theis & Fortenberry (2016) calculated rotational constants for the various isotopologs of $ArOH^+$ and $NeOH^+$. However, the spectroscopic information of $HeOH^+$ is not yet available. Here, we have carried out quantum-chemical calculation by using the Gaussian 09 program to find out these rotational parameters. We computed the rotational constants and asymmetrically reduced quartic centrifugal distortion constants with the DFT B3LYP/6-311++G(d,p) level of theory, which are useful to provide the spectral information in the THz domain. Obtained ground vibrational and equilibrium values of the rotational constants and asymmetrically reduced quartic centrifugal distortion constants along with the ground vibrational and equilibrium values calculated by Theis & Fortenberry (2016) for comparison are given in Table B1. Moreover, we used the SPCAT (Pickett 1991) program to find out the rotational transitions of these species, which fall in between the THz domain. We have supplied the obtained spectral information files on Zenodo under a Creative Commons Attribution license: doi:10.5281/zenodo.3998450. As per the JPL catalog style, we renamed the cat files of $^{36}ArOH^+$ as c053009.cat, $^{38}ArOH^+$ as c055003.cat, $^{40}ArOH^+$ as c057004.cat, $^{20}NeOH^+$ as c037006.cat, $^{22}NeOH^+$ as c039007.cat, and $HeOH^+$ as c021003.cat. For the preparation of the spectral information for $ArOH^+$ and $NeOH^+$, we used both the ground vibrational and equilibrium values of the rotational constants calculated by Theis & Fortenberry (2016), whereas, in the case of $HeOH^+$, we used our calculated parameters. For the preparation of the collisional data file, we considered the interaction between their first 11

Table B1
Ground Vibrational and Equilibrium Rotational Constants and Asymmetrically Reduced Quartic Centrifugal Distortion Constants of $ArOH^+$, $NeOH^+$, and $HeOH^+$ with the DFT B3LYP/6-311++G(d,p) Level of Theory

Sl. No.	Species	Rotational Constants	Calculated Values (in MHz)	Distortion Constants	Calculated Values (in MHz)
1.	$^{36}ArOH^+$ (Singlet)	A_0	606170.618 (574419.7[a])	D_N	0.026258855
		B_0	13423.202 (14538.2[a])	D_K	2846.358531040
		C_0	12929.814 (14157.4[a])	D_{NK}	30.956851344
		A_e	568404.429 (577984.9[a])	d_N	-0.001548795
		B_e	13362.883 (14652.2[a])	d_K	7.374941060
		C_e	13055.944 (14290.0[a])		
2.	$^{38}ArOH^+$ (Singlet)	A_0	607114.959 (574400.2[a])	D_N	0.025404061
		B_0	13198.879 (14293.6[a])	D_K	2929.193961459
		C_0	12717.473 (13925.4[a])	D_{NK}	30.950234568
		A_e	568391.892 (577970.7[a])	d_N	−0.001507393
		B_e	13137.742 (14405.4[a])	d_K	7.371572618
		C_e	12840.938 (14055.1[a])		
3.	$^{40}ArOH^+$ (Singlet)	A_0	608006.144 (574382.6[a])	D_N	0.024644498
		B_0	12996.499 (14073.0[a])	D_K	3007.592807161
		C_0	12525.768 (13715.9[a])	D_{NK}	30.944237144
		A_e	568380.591 (577958.0[a])	d_N	−0.001470202
		B_e	12934.645 (14182.7[a])	d_K	7.368596645
		C_e	12646.841 (13843.0[a])		
4.	$^{20}NeOH^+$ (Singlet)	A_0	523937.941 (525452.4[a])	D_N	0.095861623
		B_0	18963.535 (19702.7[a])	D_K	1279.215533495
		C_0	18045.404 (18942.7[a])	D_{NK}	38.200509306
		A_e	525035.970 (530275.0[a])	d_N	−0.002683004
		B_e	19104.672 (20252.3[a])	d_K	9.480927416
		C_e	18433.910 (19507.3[a])		
5.	$^{22}NeOH^+$ (Singlet)	A_0	524108.356 (525436.6[a])	D_N	0.088272895
		B_0	18178.763 (18884.4[a])	D_K	1366.928818198
		C_0	17320.737 (18185.1[a])	D_{NK}	38.205763489
		A_e	525022.539 (530266.0[a])	d_N	−0.002605291
		B_e	18307.032 (19406.6[a])	d_K	9.452753621
		C_e	17690.192 (18721.4[a])		
6.	$HeOH^+$ (Singlet)	A_0	526770.350	D_N	2.987029963
		B_0	108480.244	D_K	294.469427824
		C_0	88444.204	D_{NK}	78.618941712
		A_e	530435.668	d_N	0.215953242
		B_e	110472.442	d_K	24.945899641
		C_e	91430.461		

Note.
[a] Theis & Fortenberry (2016).

levels. This upper limit of the level is because of the absence of collisional rates of ArH^+ for the upper levels (Hamilton et al. 2016). Because for the case of hydroxyl ions we do not have any first-hand approximation for the collisional rates, we considered the same collisional rates for all these hydroxyl ions that were provided by Hamilton et al. (2016) for ArH^+. We considered their transitions further for the modeling. However, looking at the transitions of the first 12 levels, for the case of $ArOH^+$, we obtained the highest frequency at 318 GHz and for $NeOH^+$ at 437 GHz. These frequencies are not in the range of SPIRE or PACS. However, these transitions fall within the observed range of ALMA, IRAM 30 m, and NOEMA. In the case of $HeOH^+$, most of the frequencies that arise fall within the range of Herschel SPIRE, SOFIA, ALMA, IRAM 30 m, and NOEMA.

Appendix C
Model B

For the modeling of the Crab H_2 emitting knot, we follow the ionizing particle model of Richardson et al. (2013) as Model B. The adopted physical parameters and the gas-phase elemental abundances with respect to total hydrogen nuclei in all forms are summarized in Tables 1 and 2 for Model B. For detailed information, please see Sections 2 and 4.2.2. The results obtained using Model B are shown in Figures C1–C6.

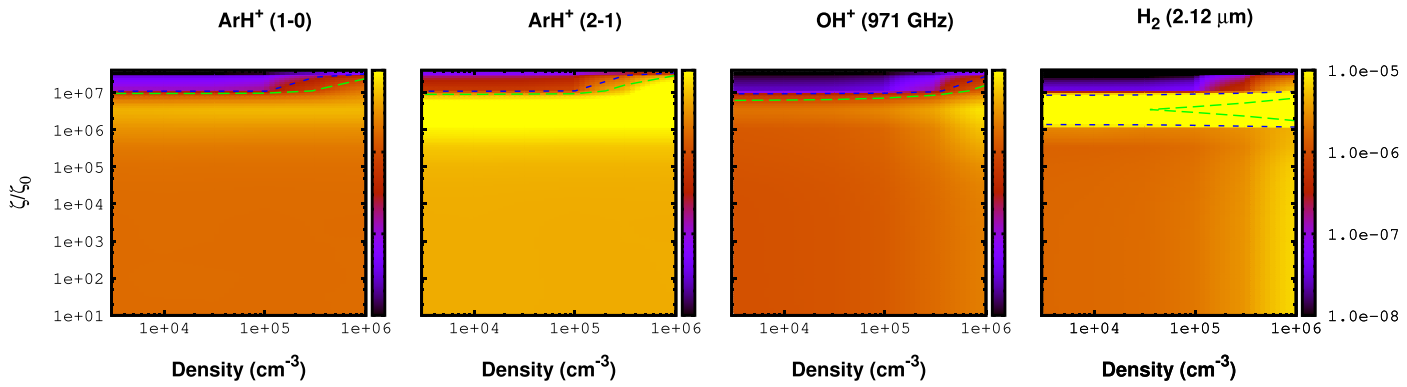

Figure C1. Parameter space for the intrinsic line surface brightness (SB) of the 1−0 and 2−1 transitions of ArH^+, the 971 GHz/308 μm transition of OH^+, and the 2.12 μm transition of H_2 considering Model B. Rightmost panel is marked with color-coded values of the intrinsic line SB (in units erg cm^{-2} s^{-1} sr^{-1}). The contours are highlighted in the range of observational limits noted in Table 6 (column 2).

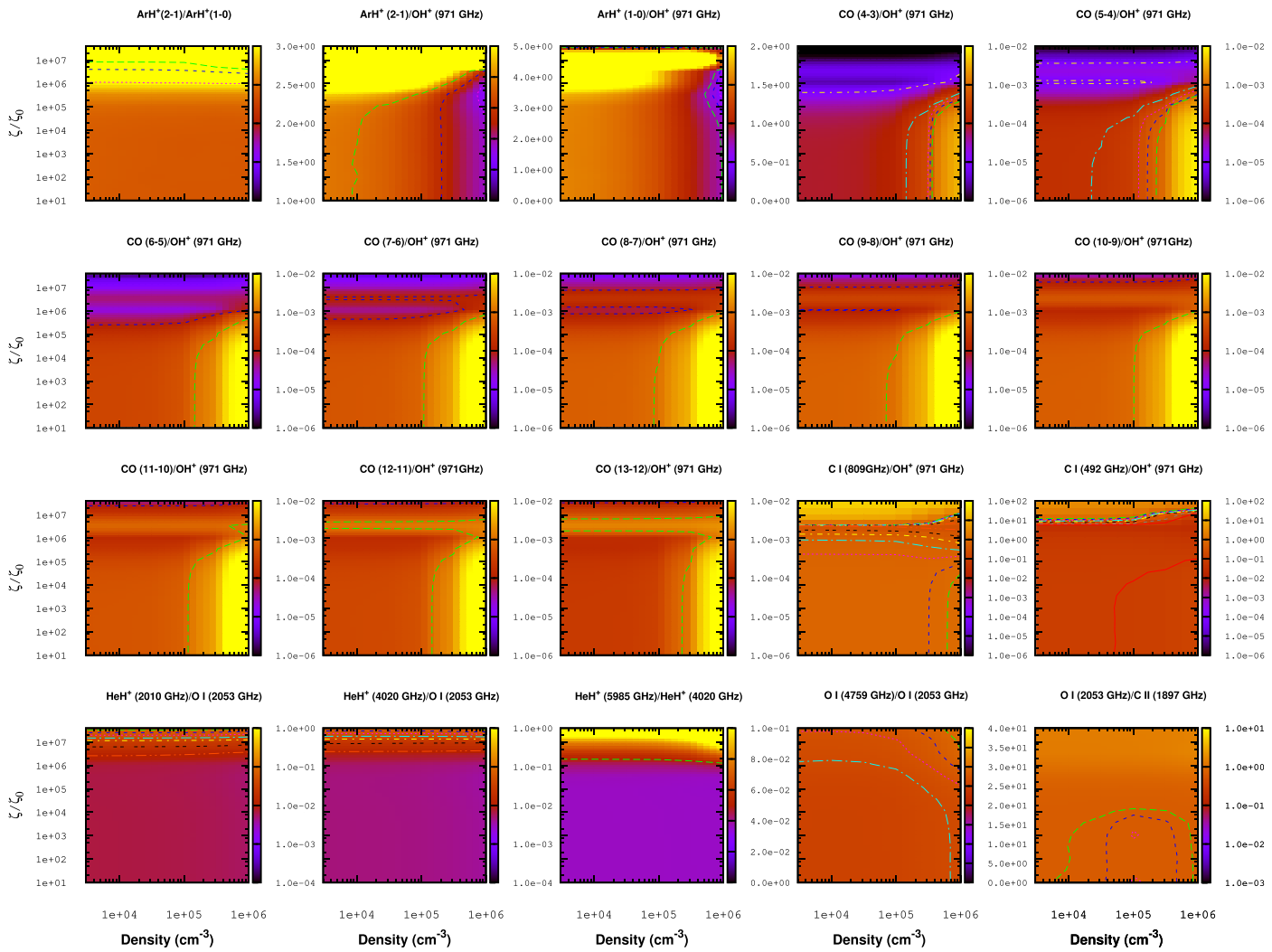

Figure C2. Intrinsic line surface brightness ratio of various molecular and atomic transition fluxes considering Model B. Contours are highlighted around the observed or previously estimated values shown in Table 7.

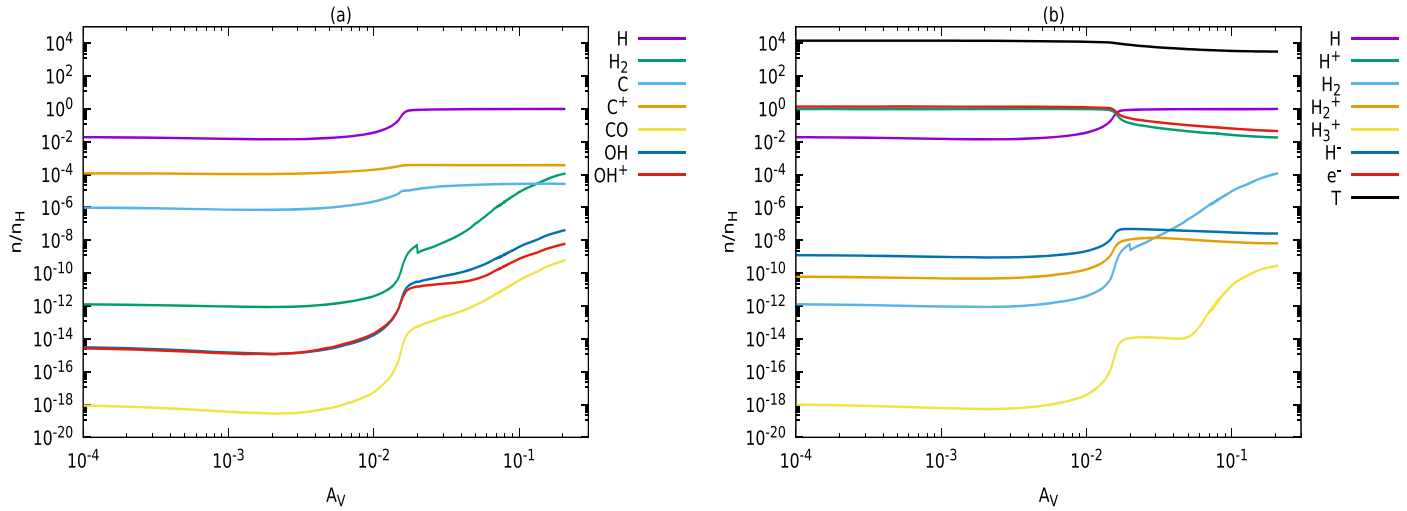

Figure C3. Abundance variation of simple species with A_V considering Model B.

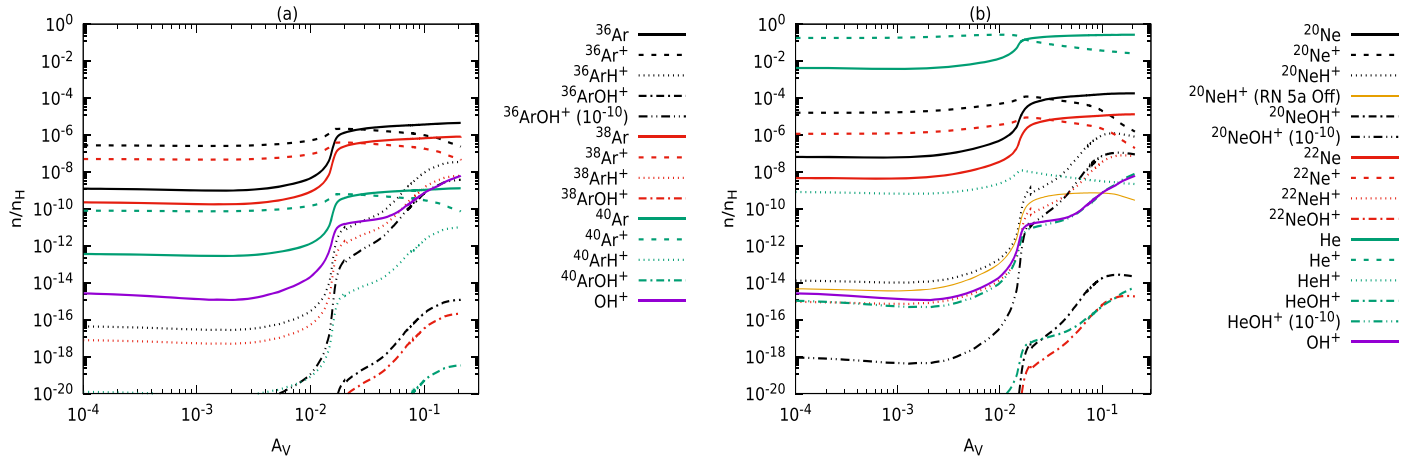

Figure C4. Abundance variation of all the hydride and hydroxyl cations considered in this work by considering Model B. In the left panel, Ar-related ions are shown, whereas in the right panel, the cases of Ne and He are shown both along with OH^+ for comparison.

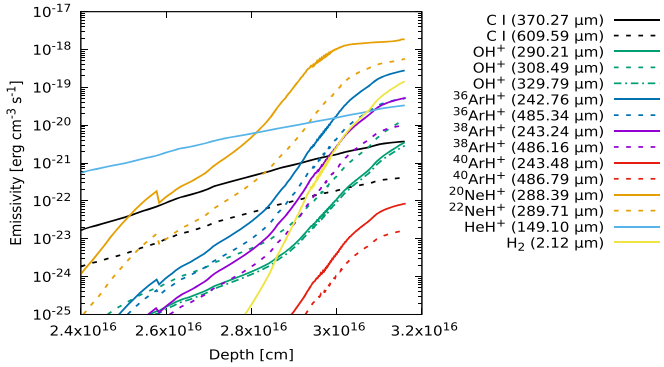

Figure C5. Emissivity of some of the strongest transitions that fall in the frequency limit of Herschel's SPIRE and PACS spectrometer and of SOFIA with respect to the depth into the filament by considering Model B.

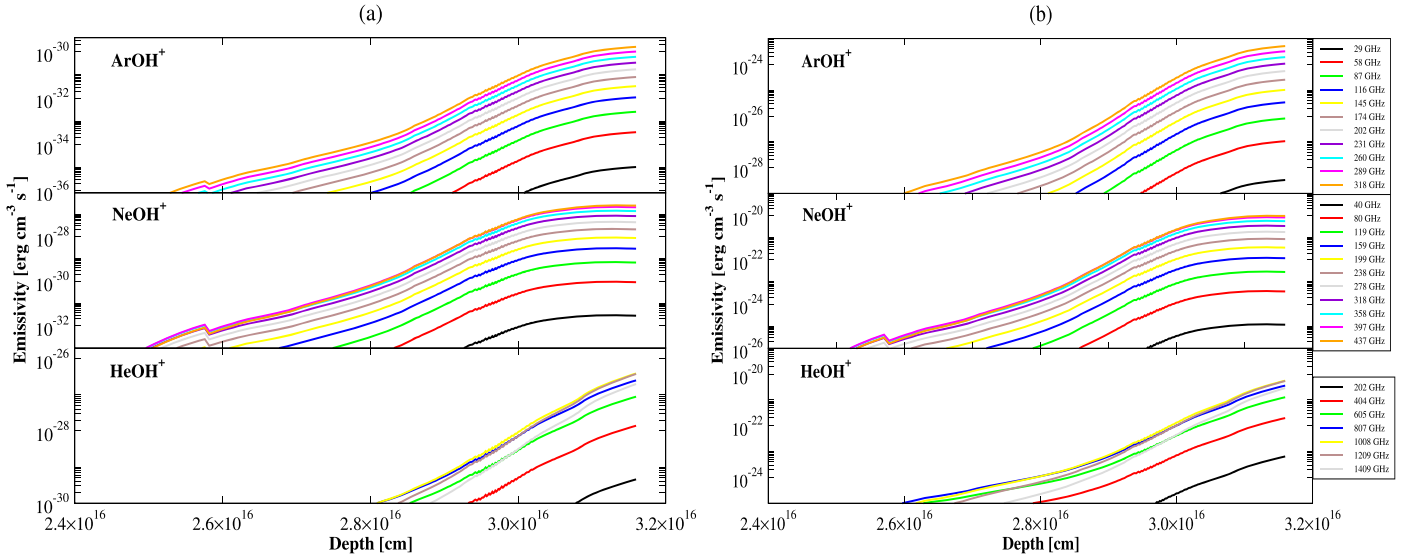

Figure C6. Calculated emissivity of various XOH^+ transitions (X = ^{36}Ar, ^{20}Ne, and He) lying in the frequency limit of Herschel's SPIRE and PACS spectrometer, SOFIA, ALMA, VLA, IRAM 30 m, and NOEMA by considering Model B. (a) Emissivity considering the formation rates following Bates (1983), mentioned in Section 3.3, whereas (b) considers the upper limit of $\sim 10^{-10}$ cm^3 s^{-1}.

ORCID iDs

Ankan Das https://orcid.org/0000-0003-4615-602X
Milan Sil https://orcid.org/0000-0001-5720-6294
Bratati Bhat https://orcid.org/0000-0002-5224-3026
Prasanta Gorai https://orcid.org/0000-0003-1602-6849
Sandip K. Chakrabarti https://orcid.org/0000-0002-0193-1136
Paola Caselli https://orcid.org/0000-0003-1481-7911

References

Abdoulanziz, A., Colboc, F., Little, D. A., et al. 2018, MNRAS, 479, 2415
Barlow, M. J., Swinyard, B. M., Owen, P. J., et al. 2013, Sci, 342, 1343
Bates, D. R. 1983, ApJ, 270, 564
Bayet, E., Williams, D. A., Hartquist, T. W., & Viti, S. 2011, MNRAS, 414, 1583
Bell, T. A., Roueff, E., Viti, S., & Williams, D. A. 2006, MNRAS, 371, 1865
Bell, T. A., Viti, S., Williams, D. A., Crawford, I. A., & Price, R. J. 2005, MNRAS, 357, 961
Bertoldi, F., & Draine, B. T. 1996, ApJ, 458, 222
Biham, O., Furman, I., Pirronello, V., & Vidali, G. 2001, ApJ, 553, 595
Black, J. H. 1978, ApJ, 222, 125
Cazaux, S., & Tielens, A. G. G. M. 2002, ApJL, 575, L29
Cazaux, S., & Tielens, A. G. G. M. 2004, ApJ, 604, 222
Cernicharo, J. 2012, in EAS Pub. Ser. 58, ECLA - European Conf. on Laboratory Astrophysics, ed. C. Stehlé, C. Joblin, & L. d'Hendecourt (Les Ulis: EDP Sciences), 251
Chakrabarti, S. K., Das, A., Acharyya, K., & Chakrabarti, S. 2006a, A&A, 457, 167
Chakrabarti, S. K., Das, A., Acharyya, K., & Chakrabarti, S. 2006b, BASI, 34, 299
Dalgarno, A., Yan, M., & Liu, W. 1999, ApJS, 125, 237
Davidson, K., & Fesen, R. A. 1985, ARA&A, 23, 119
Draine, B. T. 1978, ApJS, 36, 595
Ferland, G. J., Chatzikos, M., Guzmán, F., et al. 2017, RMxAA, 53, 385
Ferland, G. J., Korista, K. T., Verner, D. A., et al. 1998, PASP, 110, 761
Fraser, M., & Boubert, D. 2019, ApJ, 871, 92
Frisch, M. J., Trucks, G. W., Schlegel, H. B., et al. 2013, Gaussian 09 Revision D.01 (Wallingford, CT: Gaussian, Inc.)
Galli, D., & Palla, F. 2013, ARA&A, 51, 163
García-Vázquez, R. M., Márquez-Mijares, M., Rubayo-Soneira, J., & Denis-Alpizar, O. 2019, A&A, 631, A86
Gomez, H. L., Krause, O., Barlow, M. J., et al. 2012, ApJ, 760, 96
Güsten, R., Wiesemeyer, H., Neufeld, D., et al. 2019, Natur, 568, 357
Hamilton, J. R., Faure, A., & Tennyson, J. 2016, MNRAS, 455, 3281
Hester, J. J. 2008, ARA&A, 46, 127
Hogness, T. R., & Lunn, E. G. 1925, PhRv, 26, 786
Indriolo, N., Neufeld, D. A., Gerin, M., et al. 2012, ApJ, 758, 83
Jolly, W. L. 1984, Modern Inorganic Chemistry (New York: McGraw-Hill)
Jura, M. 1975, ApJ, 197, 575
Kamrukov, A., Kozlov, N., Protasov, Y. S., & Chuvashev, S. 1983, OptSp, 55, 9
Kaplan, D. L., Chatterjee, S., Gaensler, B. M., & Anderson, J. 2008, ApJ, 677, 1201
Kingdon, J. B., & Ferland, G. J. 1996, ApJS, 106, 205
Lee, J.-Y., Marti, K., Severinghaus, J. P., et al. 2006, GeCoA, 70, 4507
Lennon, M. A., Bell, K. L., Gilbody, H. B., et al. 1988, JPCRD, 17, 1285
Lepp, S., Stancil, P. C., & Dalgarno, A. 2002, JPhB, 35, R57
Loh, E. D., Baldwin, J. A., Curtis, Z. K., et al. 2011, ApJS, 194, 30
Loh, E. D., Baldwin, J. A., & Ferland, G. J. 2010, ApJL, 716, L9
Loh, E. D., Baldwin, J. A., Ferland, G. J., et al. 2012, MNRAS, 421, 789
Lord, S. D. 1992, A New Software Tool for Computing Earth's Atmospheric Transmission of Near-and Far-infrared Radiation, NASA Technical Memorandum 103957 (Moffett Field, CA: NASA Ames Research Center), https://ntrs.nasa.gov/citations/19930010877
Meijerink, R., & Spaans, M. 2005, A&A, 436, 397
Meshik, A., Mabry, J., Hohenberg, C., et al. 2007, Sci, 318, 433
Müller, H. S. P., Muller, S., Schilke, P., et al. 2015, A&A, 582, L4
Müller, H. S. P., Schlöder, F., Stutzki, J., & Winnewisser, G. 2005, JMoSt, 742, 215
Müller, H. S. P., Thorwirth, S., Roth, D. A., & Winnewisser, G. 2001, A&A, 370, L49
Neufeld, D. A., Goto, M., Geballe, T. R., et al. 2020, ApJ, 894, 37
Neufeld, D. A., & Wolfire, M. G. 2016, ApJ, 826, 183
Orient, O. J. 1977, CPL, 52, 264
Owen, P. J., & Barlow, M. J. 2015, ApJ, 801, 141
Pickett, H. M. 1991, JMoSp, 148, 371
Priestley, F. D., Barlow, M. J., & Viti, S. 2017, MNRAS, 472, 4444
Richardson, C. T., Baldwin, J. A., Ferland, G. J., et al. 2013, MNRAS, 430, 1257
Roberge, W., & Dalgarno, A. 1982, ApJ, 255, 489
Roueff, E., Alekseyev, A. B., & Le Bourlot, J. 2014, A&A, 566, A30
Schilke, P., Neufeld, D. A., Müller, H. S. P., et al. 2014, A&A, 566, A29
Schöier, F. L., van der Tak, F. F. S., van Dishoeck, E. F., & Black, J. H. 2005, A&A, 432, 369
Shaw, G., Ferland, G. J., Abel, N. P., Stancil, P. C., & van Hoof, P. A. M. 2005, ApJ, 624, 794
Shull, J. M., & van Steenberg, M. 1982, ApJS, 48, 95
Stäuber, P., Doty, S. D., van Dishoeck, E. F., & Benz, A. O. 2005, A&A, 440, 949
Sternberg, A., & Neufeld, D. A. 1999, ApJ, 516, 371
Theis, R. A., & Fortenberry, R. C. 2016, MolAs, 2, 18
Theis, R. A., Morgan, W. J., & Fortenberry, R. C. 2015, MNRAS, 446, 195

Trimble, V. 1968, PhD thesis, Caltech
van der Tak, F. F. S., Black, J. H., Schöier, F. L., Jansen, D. J., & van Dishoeck, E. F. 2007, A&A, 468, 627
Verner, D. A., & Yakovlev, D. G. 1995, A&AS, 109, 125
Wieler, R. 2002, RvMG, 47, 21
Zicler, E., Parisel, O., Pauzat, F., et al. 2017, A&A, 607, A61
Zubko, V. G., Mennella, V., Colangeli, L., & Bussoletti, E. 1996, MNRAS, 282, 1321